TUTORIAL REVIEW

Check for updates

Ultrathin 2D metallenes for energy storage: a myth or reality?

Jayesh Cherusseri, [ID] *[a] Susmi Anna Thomas [ID] [b] and Deepthi N. Rajendran [ID] [b]

Rapid depletion of fossil fuels and increased energy scarcity have paved the way for the use of electrochemical energy storage devices, such as rechargeable batteries and supercapacitors, to power electronic devices. Ultrathin two-dimensional (2D) materials have attracted significant research interest due to their prominent characteristics, including large surface area, lightweight, good electronic conductivity, and good chemical and electrochemical properties. Metallenes are emerging class of 2D materials with an atomic thickness and consisting of metals or alloys with a well-controlled surface atomic arrangement. 2D metallenes are invariably used as electrode-active materials in energy storage devices such as rechargeable batteries and supercapacitors in the literature. Since metallenes consist of

[a]Department of Chemistry (BK21 FOUR), Research Institute of Advanced Chemistry, Gyeongsang National University, Jinju 52828, Republic of Korea. E-mail: drjayeshpuli@gmail.com

[b]Department of Physics, Government College for Women (Affiliated to University of Kerala), Thiruvananthapuram, Kerala 695014, India

Jayesh Cherusseri completed his master's degree (MSc) in physics, followed by a master's degree (MTech) in nanomedical sciences. He obtained a PhD with a distinction in materials science from the Indian Institute of Technology (IIT) Kanpur, India, in 2017. He was a recipient of Dr D. S. Kothari post-doctoral fellowship from India in 2017 and the University of Central Florida (UCF) post-doctoral fellowship in 2018. He has more than 100 research publications including research articles and book chapters to his credit. He holds an h-index of 32 and an i10-index of 59, with more than 3500 citations. He has two Indian and one US patent to his credit. He was a recipient of the prestigious Brainpool Fellowship from NRF South Korea in 2024. Dr Cherusseri is currently working as a Brainpool Fellow at Gyeongsang National University, Jinju, South Korea. He was listed in the Stanford University/Elsevier's List of Top 2% Scientists in the World. He is a reviewer of several top-listed journals in the world, such as Nature Communications, Advanced Materials, ACS Nano, Progress in Materials Science, Journal of Energy Chemistry, etc. His current research focuses on the synthesis and electrochemical applications of new-generation ultrathin materials.

Jayesh Cherusseri

Susmi Anna Thomas is a PhD scholar at the Department of Physics, Government College for Women, Thiruvananthapuram, affiliated to the University of Kerala, Thiruvananthapuram, Kerala, India. She completed her master of science (MSc) degree with a specialization in physics in 2018 from Mar Ivanios College, Thiruvananthapuram (Affiliated to University of Kerala), Kerala, India. She also obtained a master of philosophy (MPhil) in physics (University First Rank Holder) from the Noorul Islam Centre for Higher Education, Tamil Nadu, India, in 2020. Dr Thomas is a recipient of prestigious INUP project awarded by the Ministry of Electronics and Information Technology (MeitY), Government of India, for carrying out the experimental work at Centre for Nano Science and Engineering (CeNSE), Bangalore during her PhD. She has published more than 38 research articles and 9 book chapters with an h-index of 17 with an i10-index of 29, having more than 800 citations. Her current research focuses on the development of new-generation two-dimensional layered materials, like transition metal chalcogenides and their applications in electrochemical energy storage devices such as rechargeable batteries and supercapacitors. She is a reviewer of several top listed peer-reviewed journals such as Journal of Energy Storage, Journal of Alloys and Compounds, ACS Applied Energy Materials, etc.

Susmi Anna Thomas

metallic 2D sheets, charge storage is limited by electrode kinetics and the electrode is more prone to corrosion when used in electrolytes. This motivated us to examine the truth behind these fascinating materials. We critically analysed the various types of metallenes available to date, their synthesis methods, and the mechanism of charge storage in rechargeable batteries and supercapacitors for better clarification.

Sustainability spotlight

The current energy demand requires sustainable and renewable electrochemical energy storage devices with features such as mobility, high specific energy, low cost, and safety. Electrochemical energy storage devices, such as rechargeable batteries and supercapacitors, use nanostructured electrode-active materials for charge storage. Metallenes-based electrodes are a versatile option for developing sustainable batteries and supercapacitors. These devices will achieve the UN Sustainable Development Goal 7: Affordable and clean Energy. Metallenes-based electrodes may revolutionize the world of sustainable electrochemical energy storage devices because they are robust, stable, low-cost, high performance and safe to use.

1. Ultrathin 2D metallenes

Ultrathin two-dimensional (2D) layered materials have received significant research interest due to their large surface area, suitable plane for charge transfer and quantum-size effects.[1–4] After the discovery of graphene, research has been conducted to synthesize various types of 2D materials, with conductivity spans from an insulator to a semiconductor toward conductors.[5–7] 2D materials are different from their bulk counterparts in terms of properties.[8,9] The peculiar properties of 2D materials such as physical, chemical, optical, electronic, thermal, and mechanical properties enabled them to be utilized in a variety of applications, including catalysis, energy storage, and sensors.[10,11] Almost hundreds of 2D materials have been explored to date, and some examples are transition metal dichalcogenides,[12–14] layered double hydroxides,[15] graphitic carbon nitride,[16] and MXenes.[17,18] In the literature, materials ending with "ene" refer to ultrathin 2D materials, *e.g.*, borophene, silicene, germanene (Ge-ene), phosphorene, stanene (Sn-ene), antimonene (Sb-ene), and bismuthene (Bi-ene) to name a few. Among these, silicene and phosphorene are semiconductors, whereas borophene, Ge-ene, Sn-ene, Sb-ene, and Bi-ene are considered metallenes. A "metallene" is a hypothetical class of materials that would be analogous to graphene but are composed of metals or alloys. Metallenes are good conductors of electricity with thicknesses in the range of one or several atomic layers.

In comparison with other metals that are widely used, metallenes have high conductivity and they are highly promising materials for catalysis, supercapacitors, and batteries.[19] Beyond other non-2D materials and their bulk counterparts of metals, metallenes possess extraordinary properties ranging from conductivity to superconductivity.[20] Atomically thin architecture of metallenes exhibits a large surface-area-to-volume ratio, which facilitates coordination with other atoms through unsaturated metal atoms present on the surface and edge sites. In comparison with surface atoms, coordinated edge atoms are unsaturated due to the formation of defects and dislocations, thereby achieving high electrochemical activity for electrochemical energy storage.[21–23] Metallenes have a higher percentage of surface unsaturated metal sites that behave as active sites, making them an efficient candidate for energy storage applications.[9] Large specific surface area and increased surface energy (as it promotes greater number of active sites) of metal atoms promote adsorption mechanisms, making them suitable for ubiquitous charge storage. The ultrathin feature of metallenes reduces the diffusion distance of electrolyte ions in the electrolyte medium. Beyond these features, the capability for surface functionalization of metallenes allows tuning their electronic structure, electrochemical stability, and hydrophilicity.[14]

Although metallenes possess several advantages, research on metallenes is still in its infancy. The thermodynamic instability and limited synthesis routes available make their application limited. Hence, obtaining a free-standing layer remains a challenge in the case of metallenes.[24] To demonstrate the wide acceptability of the metallenes as ultrathin materials for energy storage applications, we planned to investigate the truth behind the acceptability of this class of materials. The statistical representation of number of publications related to metallenes is shown in Fig. 1. The number of citations received for these publications in each year is presented as an inset graph in

Deepthi N. Rajendran

Deepthi N. Rajendran completed her master's degree (MSc) in physics, followed by master of philosophy in physics from University of Kerala, Thiruvananthapuram, Kerala, India. She obtained her PhD in physics from the University of Kerala, India, in 2007. She has published more than 60 research publications to date. Her current research focuses on the development of nanomaterials for energy applications, especially in solid oxide fuel cells and supercapacitors. Dr Deepthi is currently working as an associate professor and research guide at the Department of Physics, Government College for Women, Thiruvananthapuram, Kerala, India. Seven PhDs were produced under her guidance and five students are presently pursuing PhD under her supervision.
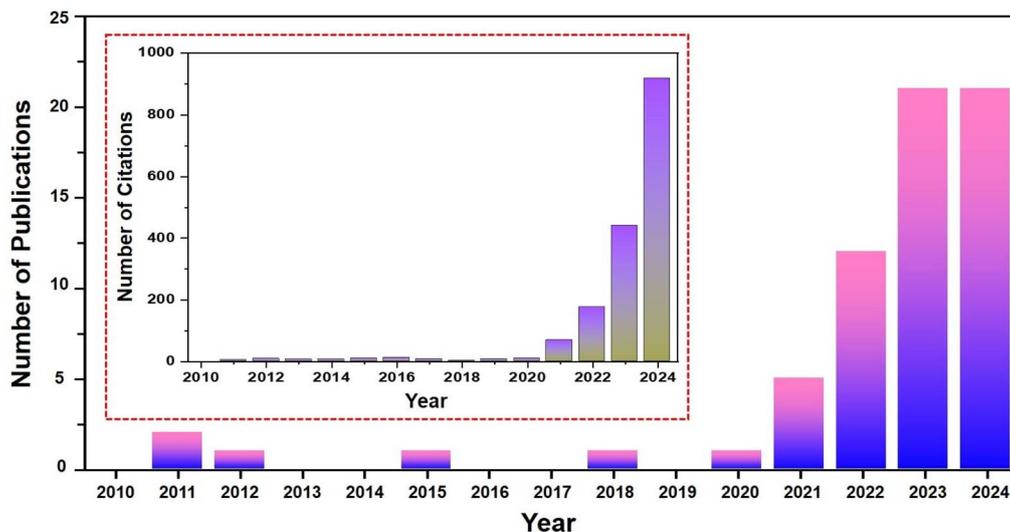
Fig. 1 Number of publications (inset: number of citations received in each year) related to metallenes for the past 15 years (source: web of science; keyword: "metallenes").

Fig. 1. From this graphical representation, it can be observed that there exists only a very small number of publications and studies with respect to metallenes in the literature, but a rapid increase in research related to metallenes can be observed over the past 5 years.

The depletion of fossil fuel resources and the ever-increasing global population have led to a severe energy crisis. Although various renewable energy conversion technologies have been developed, such as solar cells, windmills, and tidal turbines, their intermittent nature necessitates the need for energy storage technologies. Among the various choices available, the most promising energy storage is electrochemical energy storage. This includes capacitors, batteries, and super-capacitors. Conventional capacitors or dielectric capacitors are good candidates for high power density, but very low energy density. On the other hand, supercapacitors exhibit high specific capacitance, high power density and moderate energy density. Batteries are the most common examples of electro-chemical energy storage devices that are used in daily life. Rechargeable batteries, such as metal–ion batteries,[25] metal–sulfur batteries,[26] and metal–air batteries,[27] are the most extensively explored battery types. Electrode and electrolyte materials play crucial roles in determining the voltage window and electrochemical performance of batteries and super-capacitors.[28,29] Detailed reviews of various advanced materials for energy-storage applications are available in the literature. However, the salient features of using 2D metallenes in energy storage have not been explored to date. This motivated us to ask the following research question: "Ultrathin 2D metallenes for energy storage is a myth or reality?". This review critically evaluates the salient features of metallenes capable of use in energy storage applications such as supercapacitors and batteries. We review the fundamental properties of metallenes, their synthesis routes and their exemplary applications in the field of electrochemical energy storage.

2. 2D metallenes for supercapacitors

There are different types of metallenes explored to date, most of which have been explained theoretically, and only a small number have been experimentally investigated. After the discovery of graphene in the year 2004, it became a fascinating material of choice for many electronic device applications due to its tunability in the electronic structure, number of layers, and surface functionalization. Graphene and its derivatives are invariably used in energy storage because of their unique features, such as 2D architecture, large surface area, good chemical and electrochemical stabilities, and good capacity.[30] Graphene is a perfect choice for semiconducting devices, whereas metallenes are not suitable because of their zero bandgap.[31] However, ligand-functionalized metallenes may be complementary to graphene in the future.[32] Ge-ene-based materials received prominent attention in the field of electro-chemical energy storage, particularly for electric double-layer capacitors (EDLCs). Similar to graphene, monolayered Ge-ene has a honeycomb buckling structure, which can store charges *via* the formation of a double layer, as theoretically studied. Researchers have conducted simulation studies such as hydrogenation, functionalization, organic functional group termination, and exogenous doping of elements. From these studies, it is observed that the physical and chemical features of Ge-ene can be altered.[19] A recent study comprising experimental and theoretical analysis of low-dimensional materials such as carbon nanotubes and graphene unveils that the overall inter-face capacitance is a series combination of a double-layer capacitance and quantum capacitance (C_Q).[33] From this study, it is clear that C_Q has a significant influence on the total capacitance. At a reduced applied potential, the C_Q of graphene limits the performance of EDLC. A variation in the C_Q affects the overall capacitance of the electrode-active material. Xu *et al.*[33] evaluated the C_Q of pristine and defect-induced Ge-ene through

first-principle calculations with the aid of a projected augmented wave potential approach using the Vienna *Ab initio* Simulation Package. In this study, the exchange-correlation energy of the interacting electrons were obtained by a generalized gradient approximation functional with the Perdew–Burke–Ernzerhof (PBE) functional. Here, the integral *k*-space and the plane wave basis set with a cut-off energy of 450 eV are properly selected to achieve overall convergence of the energy at 1 meV per level. Here, a Monkhorst–Pack with a higher *k*-point density is used to evaluate *k*-points in the Brillouin region. Using sp³/sp² hybridization, the buckled honeycomb structure held by Ge-ene holds a lattice constant of 3.84 Å with a Ge–Ge bond length of 2.268 Å. The authors of this work observed that pristine Ge-ene exhibits linear dispersion near the Fermi level with a Dirac point, the same as that of graphene. A Stone–Wales defect (SW defect) makes Ge-ene to have a linear dispersion

near the Fermi level, breaking the degenerate state near the Γ region. In comparison with the density of states of bulk Ge-ene, for the SW defect, there exists a peak at 0.3 eV above the Fermi level (or the Dirac point) through the introduction of SW flat bands. These flat bands and degenerated states breaking near Γ reveal that there exists a partial distortion in the network of states due to Ge atom p(z) hybridization. Thus, it produces a quasi-localization state near the SW defect. The injected charge carriers gather near the Ge ring pentagon–heptagon, which is introduced from the decomposed band charge density isosurface. Moreover, a state near Γ point indicates a higher number of additional charges distributed in the Ge crystal lattice. The C_Q values of the pristine and six different defective Ge-ene electrodes were further evaluated at a temperature of 300 K, as shown in Fig. 2a–f. The C_Q profile of each Ge-ene electrode is similar to the density of state shape in thermal
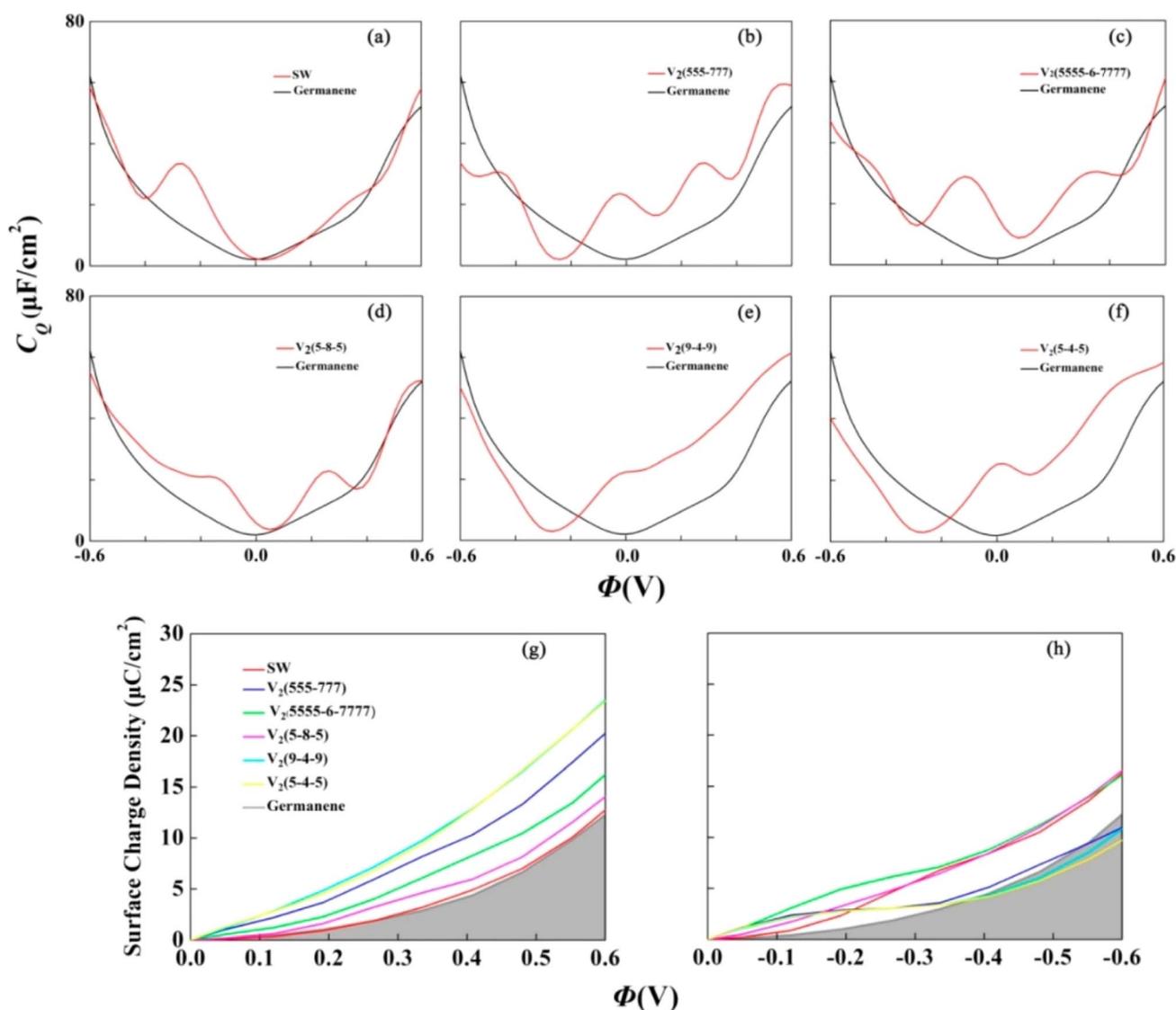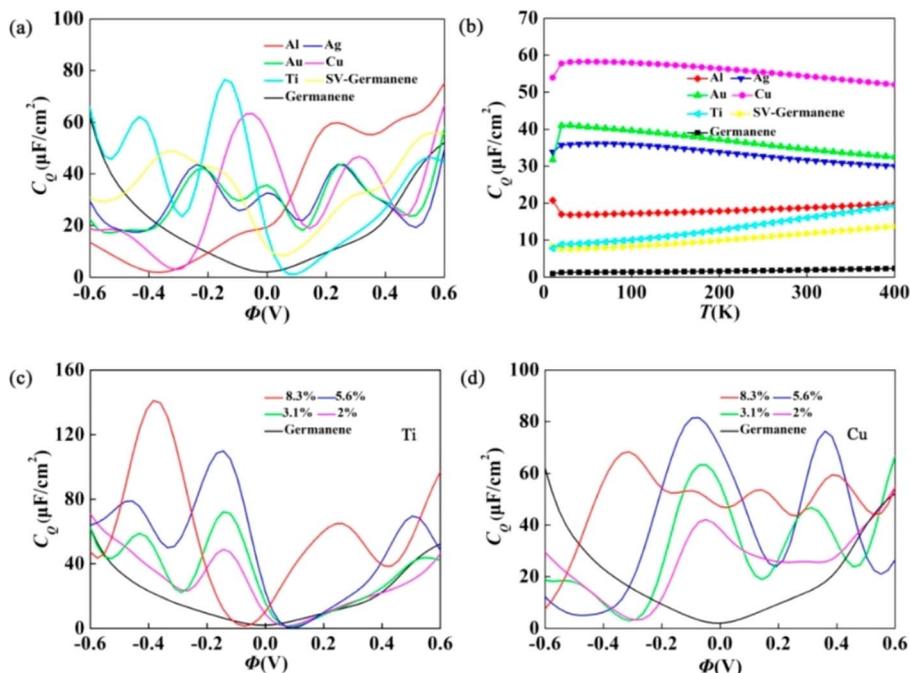

Fig. 2 (a–f) C_Q for pristine Ge-ene and defective Ge-ene; (g and h) surface charge density variation with respect to potential drop having Φ in the range of 0.0 to 0.6 V and −0.6 to 0.0 V. The results were evaluated in the supercell 6 × 6 and it possesses a defect concentration of 1.39%. Reproduced with permission from ref. 33. Copyright (2020), the American Chemical Society.

Fig. 3 (a) Calculated C_Q of the SV Ge-ene with the given elements adsorbed and the SV Ge-ene with respect to the local electrode potential (Φ); (b) change in C_Q over the temperature range of 0–400 K; calculated C_Q of the SV Ge-ene with respect to (c) Ti and (d) Cu doping with concentrations of 2%, 3.1%, 5.6%, and 8.3% with respect to local electrode potential. Reproduced with permission from ref. 33. Copyright (2020), the American Chemical Society.

broadening. The C_Q is increased with an increase in $|\Phi|$ and it reaches 60 μF cm^{-2} at $\Phi = \pm 0.6$ V for the pristine Ge-ene. For all six defect-induced Ge-ene electrodes, a higher irregular C_Q was observed near the neutrality point. The C_Q of pristine Ge-ene significantly increases, and this peak corresponds to the above-mentioned quasi-localized p(z) state. In this present point of view, the overall accumulation of charge (Fig. 2g and h), the double vacancy (DV) defects V_2 (9–4–9) and the V_2 (5–4–5) holds an increase in effect during a positive bias, but with a negative bias, the accumulation of charges increases rapidly for defects V_2 (5555–6–7777), V_2 (5–8–5) and the SW defect.

To evaluate the electronic structure of metal-doped Ge-ene, the charge density isosurfaces with band decomposition of Ti and Cu doping were analysed. For states occupied with energy levels between the −0.5 eV and the Fermi level, the distribution of charges is intensive over the Ti (Cu) atom and the three nearby Ge atoms. In Ti doping, these proposed states originate from the Ge p(z) and Ti 3d(z^2) orbital contributions. In doping Cu, these given states are introduced from the Cu 3d($x^2 - y^2$) orbitals, and the Ge 4p orbital consists of p(x), p(y) and p(z). If the band is in an occupied state above the Fermi level and smaller than 0.5 eV, the given charge also makes the distribution mainly over Ti (Cu) atoms with nearby Ge atoms in the complex. In Ti doping, two groups of localized bands appear. The localized band near the Fermi level was derived from the Ge p(z) and Ti d(xy)/d($x^2 - y^2$) orbital contributions. Here, the second group present in the localized band is introduced from the Ti d(z^2) orbital. With similarity to metal-atom-doped graphene, an overlap exists between Ge quasi-sp^2 and the Ti d(xz)/d(yz) orbitals out-of-plane resulting in σ–σ* states (σ is from Ge p(x)/p(y) and σ* is from Ti d(xz) and Ti

d(yz)). In Cu doping, the Fermi level shifts down with respect to Cu 3d electron deficiency. The Cu 3d orbital does not hold any contribution from the conduction band, it arises specifically from the π* state of the Ge p(z) orbital. For the adsorption of Cu atoms on pristine Ge-ene, charges are transferred from Cu to Ge atoms, which are localized at a region near three atoms in the upper surface with higher symmetry, but for Cu doping with single vacancy (SV) Ge-ene, the introduction of chemical bonds present between the Cu and Ge atoms occurs. In the electrode's operation state, the stability of the metal adsorption system on bare Ge-ene is changed by following the injection/removal of electrons because this stability is controlled by the transfer of charges. With respect to the removal of electrons during operation, there is a reduction in the transfer of charges, and there is a decrease in the adsorption stability. During metal adsorption on SV Ge-ene, stability does not cause any prominent changes in the operation state with respect to the orbital hybridization as the primary factor. The influence of SV Ge-ene with respect to various metal adsorbates depends upon C_Q is analysed in Fig. 3a. To analyse the effect of doping on C_Q using various elements such as aluminum (Al), silver (Ag), gold (Au), copper (Cu), and titanium (Ti) on pristine and SV Ge, is shown in Fig. 3a. In the case of the SV Ge-ene, the C_Q of the pristine Ge-ene makes an improvement. This is attributed to the presence of a localized state near the Dirac point generated by metal dopant complex and SV. The localization effect of states near the Fermi energy of a doped system is evaluated by the temperature dependency of C_Q, as shown in Fig. 3b. By changing the temperature of the system in the range of 0 to 400 K, the authors of this work evaluated the C_Q at zero bias. In this case, it was observed that the pristine Ge-ene did not undergo any

changes and exhibited a value of ~1.96 μF cm^{-2}. For systems Au, Ti, Cu, Ag, and Al combined with SV, no significant change in C_Q of SV Ge-ene was observed within the temperature region. For the local electrode potential function, a change in C_Q of the Ti- and Cu-doped SV Ge-ene were observed at various concentrations is depicted in Fig. 3c and d. When the Ti concentration was increased from 2% to 8.3%, C_Q increased from 48.9 μF cm^{-2} (−0.14 V) to 141.1 μF cm^{-2} (−0.38 V). In comparison with pristine Ge-ene, the electronic structure of doped Ge-ene was not affected by a reduced dopant concentration. For a 5.6% doping concentration, C_Q reached a maximum value of 110.2 μF cm^{-2} at a temperature of 300 K in Ti-doped Ge-ene (Fig. 3c) where C_Q was evaluated with respect to Φ at various concentrations. At reduced concentrations, a localized energy state is introduced through the defects, which begin to hybridize and expand via quasi-localization phenomena.

Stanene (Sn-ene) is another member of the family, composed of a single layer of tin (Sn) atoms arranged in a 2D manner. Sn-ene exhibits prominent features like room temperature spin hall quantum effect, topological superconductivity behaviour, thermoelectricity, etc. to name a few.[34] Sn-ene monolayer can be prepared over Bi$_2$Te$_3$ (111) via molecular beam epitaxy.[34] The alloy-terminated surface was found to be a template for the growth of higher-scale Sn-ene film. Zhou et al.[35] studied the influence of vacancy-defect, doping of single-element and co-doping of multiple elements on the C_Q of Sn-ene electrodes. The authors of this work have selected two different types of dopants, such as light-element dopants (B, N, Al, Si, P, and S)

and metals such as Ti, V, Cr, Mn, Fe, and Ni. Their investigation unveiled that Sn-ene exhibits high C_Q under vacancy at 0 V. The capacitance was found to be increased with co-doping in comparison with single-atom doping. Sn-ene with a co-doped atomic framework possesses an efficient C_Q for negative potential for positive bias, suggesting that it acts as an effective cathode material for supercapacitors. The partial density of states suggest that C_Q curve shifting was mainly due to the contribution of the transition metal, the light element dopant, and the Sn atom. This study suggests that Sn-ene-based electrodes are efficient candidates for supercapacitor application.

Antimonene (Sb-ene) is another important metallene that has received great interest for electrochemical applications because of its isolation from conventional layered allotrope forms. It is possible to synthesize few-layered Sb-ene via liquid-phase exfoliation.[36] There is a modified synthesis approach that involves an initial step of ball-milling procedure conducted at 3000 rpm for a milling period of 180 minutes.[37] The initial step involves a prominent reduction in the size and homogenous maintenance of the Sb crystal's morphology. Using SEM imaging, it was confirmed that the prepared Sb power possesses uniformity in structure. To evaluate the electrochemical charge storage properties of this material, a Sb-modified screen-printed electrode (SPE) was prepared and the morphology was analysed by SEM analysis. SEM images show that Sb forms flakes with a lateral dimension of ~200–400 nm. The supercapacitor performance of the prepared electrode was evaluated in a two-electrode cell configuration using 0.5 M H$_2$SO$_4$

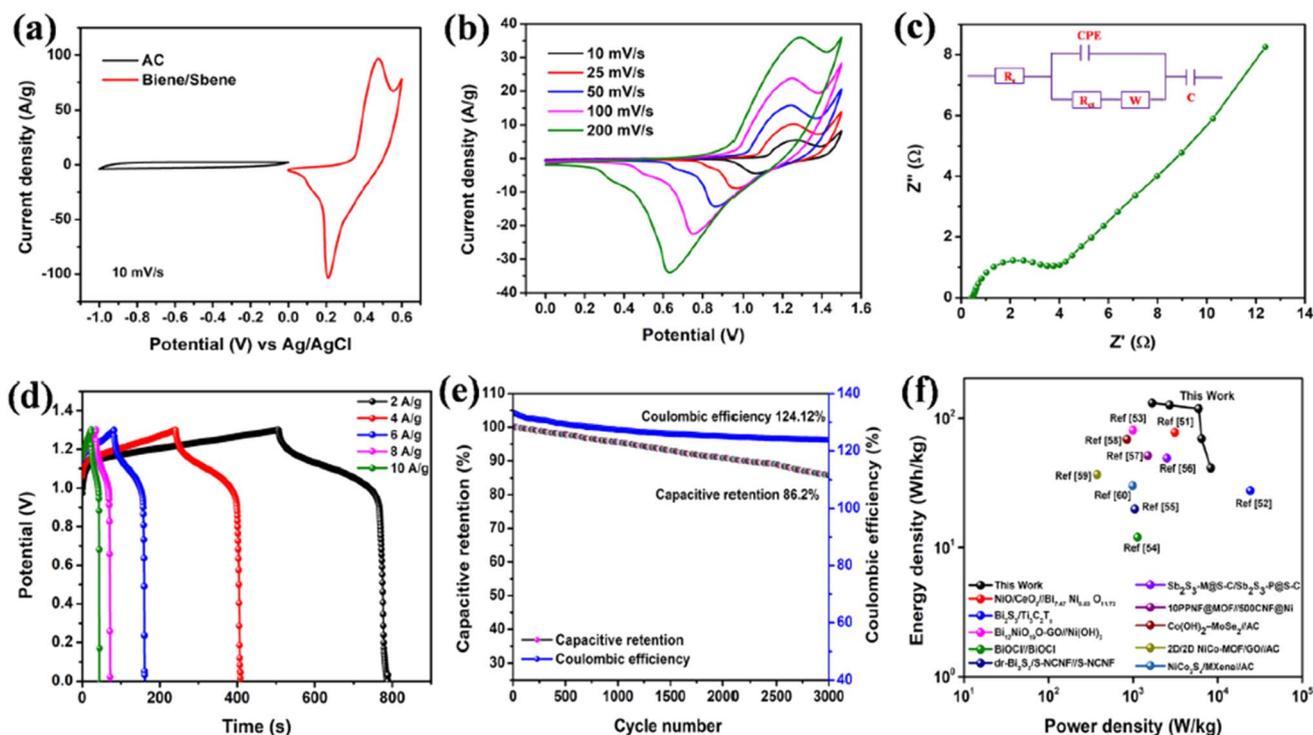**Fig. 4** (a) CV curves of AC, Bi–ene/Sb–ene at a scan rate of 10 mV s^{-1}; (b) CV curves of the HSC at different scan rates; (c) Nyquist plot of HSC (inset: equivalent circuit model); (d) GCD profiles of the HSC at different current densities; (e) capacitive retention (in %) and coulombic efficiency (in %) of the HSC; (f) comparison of the energy density and power density of the HSC with other reports in the literature. Reproduced with permission from ref. 38. Copyright (2022), the American Chemical Society.

electrolyte. The authors of his work observed both reduction and oxidation peaks in the cyclic voltammetry (CV) curves, which is due to the oxidation and reduction of Sb-ene. Hence, by faradaic phenomena, Sb-ene electrode-active material contributed to the total capacitance. The supercapacitor electrode prepared with 36 ng of Sb-ene exhibited a specific capacitance of 1578 F g^{-1} at a current density of 14 A g^{-1}. The charge/discharge stability of this electrode undergoes 1000 galvanostatic charge/discharge (GCD) cycles and achieves good capacitance retention. The supercapacitor delivered an energy density of 20 mW h kg^{-1} at a corresponding power density of 4.8 kW kg^{-1}.

A high-performing supercapacitor with bismuthine (Bi-ene)/Sb-ene was synthesized through the injection of interactions between adjacent layers through hydrogen bonding, van der Waals forces, and covalent bonds.[38] The covalent bonds between these two metallenes provide efficient combined dynamics and structural stability, which is induced through a standard liquid-phase exfoliation approach. A hybrid supercapacitor was assembled using Bi-ene/Sb-ene as the positive electrode and activated carbon (AC) as the negative electrode. The SEM image of Bi-ene shows 3D microspheres with a rough surface morphology and an average particle size of 400 nm. The exfoliated Bi-ene exhibited thin nanosheets laterally aligned with a mean lateral dimension of 120 nm. The SEM image of bulk Sb contained several cubic nanocrystals with smooth surfaces, and their diameters varied between 300 and 500 nm. The exfoliated Sb-ene consists of large nanosheets that are randomly stacked with smooth surfaces with a mean sheet length of 80 nm. There exists a random distribution of Bi-ene and Sb-ene nanosheets with perfectly defined sheet boundaries, with surfaces having a smooth morphology and a mean sheet diameter of ~100 nm. An asymmetric hybrid supercapacitor with Bi-ene/Sb-ene as the positive electrode and AC as the negative electrode was assembled with optimized potential windows of −1.0 to 0.0 V and 0.0–0.6 V, for negative and positive electrodes, respectively. The CV curves obtained at a scan rate of 10 mV s^{-1} are shown in Fig. 4a. The hybrid supercapacitor achieved an operating potential window of 0.0–1.5 V and the CV curves obtained at different scan rates are shown in Fig. 4b. Because the hybrid supercapacitor uses both an EDLC electrode and a pseudocapacitive electrode, the net charge storage is a combination of both types of mechanisms. Since the positive electrode has a 2D nanostructure, battery-type charge storage is anticipated since a higher degree of intercalation/deintercalation of electrolyte-ions between Bi-ene/Sb-ene interlayers is possible, which gives rise to an enhancement in charge storage. This in turn enhances the ionic conductivity, leading to higher electrochemical activity for an enhanced charge storage. A large area under the CV curve is an indication of amount of charge stored, as the area under the curve is directly proportional to the specific capacitance (or specific capacity in the case of supercapatteries). The high electronic conductivity of the Bi-ene/Sb-ene electrodes along with hierarchical 2D architecture are responsible for the high-rate performance of the hybrid supercapacitor. The Nyquist plot of the hybrid supercapacitor, along with the fitted equivalent circuit model as an inset image, is shown in Fig. 4c. The Nyquist plot reveals low charge transfer resistance, that eventually leads to attaining high ionic conductivity and faster ion diffusion kinetics. The series resistance (R_s) and charge transfer resistance (R_{ct}) of the
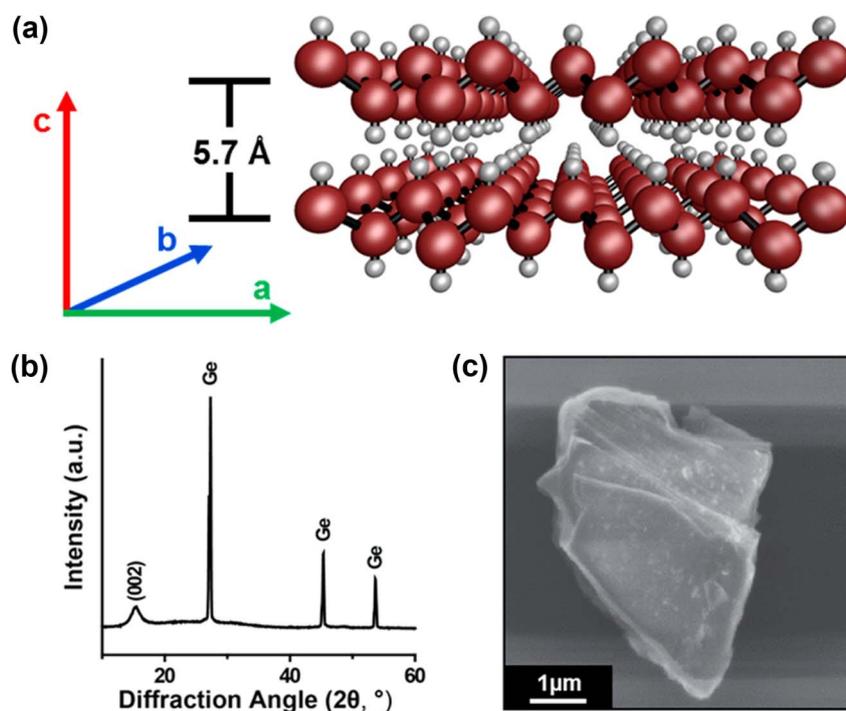

Fig. 5 (a) Pictorial representation of the stacked structure of Ge; (b) XRD spectrum of Ge, showing a stacking peak present at ~15.4° and other peaks represent characteristic Ge elemental impurities; (c) SEM image of Ge. Reproduced with permission from ref. 41. Copyright (2017), the American Chemical Society.

hybrid supercapacitor were 0.438 and 3.372 Ω, respectively. The GCD curves obtained at different current densities for the hybrid supercapacitor are shown in Fig. 4d. The hybrid supercapacitor exhibits a specific capacity of 560 and 176 C g^{-1} at a current density of 2 and 10 A g^{-1}, respectively. This supercapacitor exhibits a capacitive retention of 86.2% after 3000 charge/discharge cycles with a coulombic efficiency of 124.12%, as shown in Fig. 4e. The supercapacitor delivered an energy density of 131.44 W h kg^{-1} with a maximum power density of 8262.2 W kg^{-1}, evident from the Ragone plot (Fig. 4f).[38]

Mariappan *et al.*[39] introduced a core-shell structured 3D nickel (Ni) core and Sb-ene dendrite as shell. This hierarchical structure was prepared *via* an electrochemical deposition technique. The Sb-ene particles were dispersed over the 3D-Ni surface after an electrochemical deposition period of 5 s. A further increase in the deposition time, such as 10 and 15 s, resulted in the generation of dendritic nanostructures of Sb-ene with varied densities. The electrochemical performance of the supercapacitor electrode synthesized at a deposition period of 15 s exhibited higher specific capacitance despite the dense dendritic structure of the electrode. The electrochemical performances of the electrode material were evaluated in a two-electrode cell arrangement using Sb-ene/Ni as the positive electrode and graphene as the negative electrode in 1 M LiOH aqueous electrolyte. The CV analyses show that there is no distortion in the curves even at higher scan rates, indicating

efficient ionic and electronic conductivity. The asymmetric supercapacitor possessed a specific capacitance of 172.6 F g^{-1} at a scan rate of 5 mV s^{-1} and delivered a higher energy density of 84.79 W h kg^{-1} with a corresponding power density of 20.6 kW kg^{-1}.

3. 2D metallenes for rechargeable batteries

2D layered metallenes have significant advantages for rechargeable batteries because of their good structural stability, large surface area, and fast intercalation/deintercalation of electrolyte-ions between the layers. The efficient synthesis of 2D metallenes, such as Ge-ene, silicene and Sn-ene has a profound interest in rechargeable batteries. Sharma *et al.*[40] evaluated the electrochemical performance of monolayered and bi-layered Ge-ene as an anode for lithium (Li)-ion batteries (LIBs) using first-principle calculation with DFT. The authors of this work observed a single-atom Li adsorption on monolayered Ge-ene. Here, the Li atom at the hexagonal ring H-site has three near-neighbour Ge atoms with a bond length of ~2.70 Å. The formation energy in this particular direction is −0.43 eV. For the adsorption with two Li atoms, there are two chances; the first one is the adsorption of both of these two Li atoms above Ge-ene and the second option is that one Li atom above and the other below the Ge-ene. In the second case, the calculated
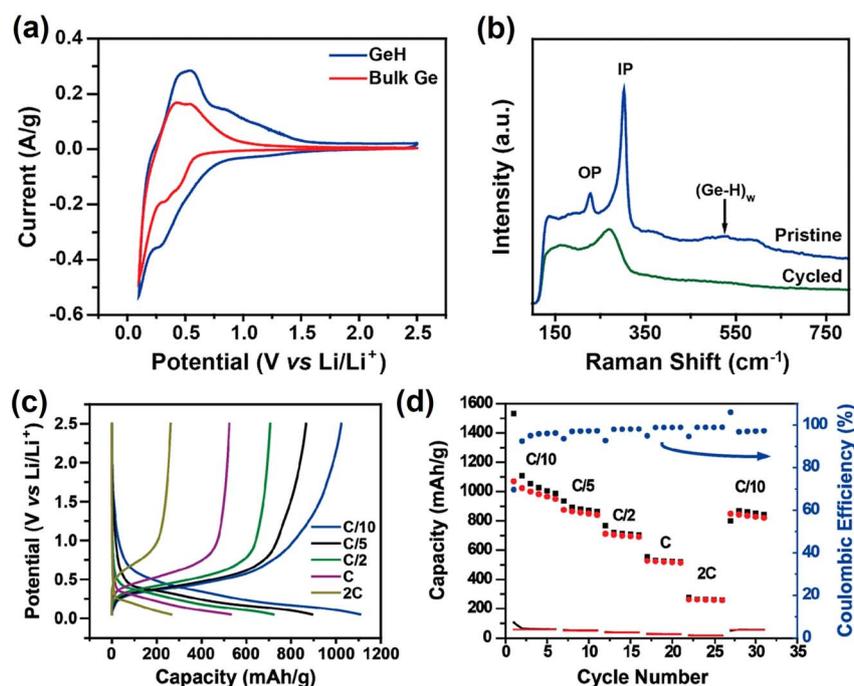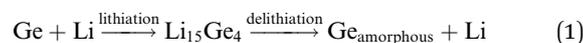

Fig. 6 (a) Comparison of CV diagrams for GeH and bulk Ge anode cycled between potentials of 2.5 and 0.1 V at a scan rate of 0.1 mV s^{-1}; (b) *ex situ* Raman spectra for pristine (blue, top) and the Li-cycled (bottom, green) Ge anode, which shows indication for change in the structure associated in the delithiation driven amorphization of GeH sheet; (c) GCD profiles for GeH anode at different charge and discharge rates within a potential window of 0.1–2.5 V *vs.* Li/Li$^+$; (d) insertion and the extraction capacity retention for GeH anode plotted with a black square and red circle, respectively, and coulombic efficiency variation with respect to cycle number plotted with blue circles. The insertion and extraction capacity contributions from the carbon fiber/carbon black and poly(acrylic acid) binder are plotted as black and red lines, respectively. Reproduced with permission from ref. 41. Copyright (2017), the American Chemical Society.

formation energy is −0.54 eV, which is smaller by 0.04 eV with respect to the first case. Thus, adsorption of greater than one Li atom over Ge-ene is more favourable. To evaluate the adsorption of Li by the bilayer Ge-ene, the same evaluation was opted as in the monolayer Ge-ene. For the single-atom case, the Li atom is adsorbed on the hexagon structure H-site, delivering a formation energy of −0.75 eV. By increasing the number of atoms, this formation energy increases when compared with single-atom adsorption of Li and attains a value of −0.70 eV for two atoms. Further increasing the number of atoms to 4, 8, and 12, the formation energy becomes −0.74, −0.79, and −0.64 eV, respectively. Using this theoretical approximation, the authors of this work found that both the monolayer and bilayer Ge-ene were covered with several Li atoms. By increasing the number of Li atoms, there exists a push nearto Ge atoms by the new Li atoms that creates a lattice distortion. To reduce the distortion of the lattice, a particular adatom is placed above the favourable adsorption site rather than in the film. Increasing the number of atoms creates numerous electronic charges around the Ge atoms. In the case of completely lithiated monolayer and bilayer Ge-ene, there exists a repulsion for further adsorption of Li atoms, and it gets stabilized thenafter. Therefore, the overall energy held by the system moves toward higher values. With the aid of this theoretical calculation, the authors found that the Li-adsorbed monolayer and bilayer Ge-ene hold a specific capacity of 369 and 276 mA h g^{-1}, respectively. A layered and stable Ge-ene hydride (GeH) was synthesized in large-scale by exfoliation and purification approach and further used as an anode material in LIBs.[41] Here, CaGe$_2$ was synthesized in an argon (Ar) atmosphere to minimize water concentration and the possible oxidation otherwise. Later, a stoichiometric quantity for Ge and calcium granules was homogeneously mixed by ball-milling and the resultant powder is loaded into an aluminum crucible and sealed in a quartz ampule under vacuum condition. Further, the as-prepared samples were annealed at a melting point greater than the individual binary elements at a temperature of 1000 °C for 24 h and allowed to cool to room temperature. The prepared product was intercalated with HCl at a temperature of −20 °C for 5 days to prepare a layered GeH. The stacked Ge layered structure is schematically shown in Fig. 5a. X-ray diffraction (XRD) analysis of CaGe$_2$ agreed with JCPDS card no. #00-013-0299. There exist calcium oxide and germanium impurities due to the higher reactivity of calcium with a trace quantity of oxygen at elevated temperatures. Calcium oxide can be easily removed by subsequent HCl etching. The XRD spectrum of layered GeH (Fig. 5b) exhibits a peak positioned at a 2θ value of ∼15.4°, which corresponds to the (002) peak, indicating an interlayer spacing of 5.7 Å. Also, the spectrum shows some indication of crystalline Ge. The SEM image of the GeH powder reveals a layered architecture with a width in the range of ∼1 μm, as shown in Fig. 5c.

The micro- and nanoscale characteristics of solution-exfoliated GeH sheets and their degree of exfoliation and degradation were measured. Exfoliated GeH sheets tend to aggregate in the dry state and show a prominent reduction in the lateral size through the forces introduced during ultra-sonication. Transmission electron microscopy (TEM) imaging shows that GeH exfoliated sheets tend to aggregate during solvent evaporation, and there exists a reduced number of isolated single sheets. Here, the polydispersed solution contains clear single sheets ranging in the lateral dimension from 40 to 200 nm, and the stacked sheets range from 40 nm to 1 μm. The authors of this work used GeH in LIBs by preparing a composite with carbon to reduce the solid electrolyte interphase (SEI) layer formation as well as to increase electronic conduction. After exfoliation, carbon nanofibers and carbon black were added to the GeH dispersion. Carbon nanofibers provide large surface areas and carbon black helps increase electronic conductivity. The as-prepared mixture was sonicated at a temperature of 15 °C for 30 minutes, and the resultant black product was drop-casted and kept for drying. After preparing the slurry, the oxygen atoms present in poly(acrylic acid) facilitate hydrogen bonding between the binder and hydrogen on the surface of GeH. The prepared slurry was subsequently introduced to a stainless steel mesh with an area of 0.5 × 0.5 cm^2 and kept for drying under vacuum at room temperature for 12 h. The fabricated electrode was folded and further pressed under a force of 10 000 lbs, resulting in an electrode thickness of <0.2 mm. The GeH mixture mass loading on electrodes was ∼3–5 mg cm^{-2}. The control sample was prepared using pure Ge powder along with carbon nanofibers and carbon black. The electrochemical analysis was performed in an Ar-filled glovebox containing an oil mixture at O level <1 ppm. The LIB cycling study was conducted using LiClO$_4$ (1.0 M) in a 95 : 5 mixture of anhydrous propylene carbonate and fluoroethylene carbonate. The use of anhydrous fluoroethylene carbonate as an additive provides an enhancement in SEI layer stability. Here, Li metal was used as the reference and auxiliary electrode. The CV curves of the exfoliated GeH and bulk Ge anodes at a scan rate of 0.1 mV s^{-1} obtained in the second cycle are shown in Fig. 6a. There exist two characteristics of the lithiation process; a broader peak present at ∼0.3 V and a steady increasing current at a low potential that terminates at the cutoff voltage of 0.1 V vs. Li/Li$^+$. The delithiation process is represented by a broader peak between 0.4 and 0.6 V vs. Li/Li$^+$. This peak corresponds to the formation of several Ge$_x$Li$_y$ phases during the insertion/deinsertion of Li. Ge lithiation follows eqn (1), and there exist several steps for lithiation, which occur at different electrochemical potentials. The entire crystalline Li$_{15}$Ge$_4$ lithiation results in amorphous Ge. A similar feature can be observed in the second CV cycle of the GeH and the bulk Ge.

$$\text{Ge} + \text{Li} \xrightarrow{\text{lithiation}} \text{Li}_{15}\text{Ge}_4 \xrightarrow{\text{delithiation}} \text{Ge}_{\text{amorphous}} + \text{Li} \qquad (1)$$

A confocal ex situ Raman spectroscopy was used to demonstrate the changes in the structural GeH after performing the electrochemical cycling study, given in Fig. 6b. Here, the GeH pristine anode possesses a characteristic peak located at 227.1 and 302.3 cm^{-1}, which corresponds to A$_1$ out-of-plane and the E$_{2g}$ in-plane vibration of Ge. The broader peak at ∼526 cm^{-1} is attributed to the (Ge–H)$_w$ vibrational mode of hydrogen. There exists an absence of hydrogen bending at ∼800 cm^{-1} or the stretching mode observed at 1890 and 1975 cm^{-1}. After

completing the cycling study, the Raman spectrum of the GeH anode exhibits a prominent change in which the A_1 out-of-plane and the E_{2g} in-plane vibration of Ge broadens and shifts toward 269.5 cm^{-1}. There exists a disappearance in the wag of a hydrogen bond at ~526 cm^{-1}, which indicates hydrogen removal through Li alloying. During this lithiation and delithiation process, there exists a change in the structural pattern, which represents the change from the crystalline order of Ge to amorphous. GCD measurements and the rate capability at different cycle numbers (Fig. 6c and d) were performed to calculate the capacity held by the composite anode of the GeH/carbon matrix at different cycling rates. For the second cycle shown in Fig. 6d, the performance of the material was accurately determined through several side reactions that occur during charging/discharging. During the initial cycles, a large change was observed in both the specific capacity and the coulombic efficiency. At a charging rate of C/10, a maximum capacity of 1108 mA h g^{-1} was observed, with a reduction in the capacity at high rates. The maximum capacity obtained for GeH lithiation and delithiation with the carbon matrix (the black

square and red circle, respectively) and the carbon matrix (black and red line, respectively) at different C rates are shown in Fig. 6d. Here, the nonzero slope as a cell voltage function represents that it does not contain any single-phase transition but instead a range of transitions, which occur at the nanoscale due to the large strain in solid Ge and Si during the lithiation process. The initial capacity of 1533 mA h g^{-1} at a rate of C/10 is higher than the theoretical capacity of GeH at room temperature. However, a large capacity distortion was observed due to the electrolyte breakdown and the formation of the SEI layer, which showed the irreversible characteristics of the anode. The irreversible redox peaks appeared at 0.54 and 0.94 for Li/Li$^+$ at a scan rate of 0.1 mV s^{-1} at the first CV cycle for GeH. The disappearance of the first reduction peak indicates the introduction of hydrogen into the total charge storage in the first cycle. After a few cycles, there exists a stabilization of capacity at ~1110 mA h g^{-1}. It exhibits a reduction in overall charge storage under the rate increase, having a capacity of 893, 720, 530, and 265 mA h g^{-1} for the C/5, C/2, 1C, and 2C, respectively. The capacity loss at high charge rates was the same as that observed
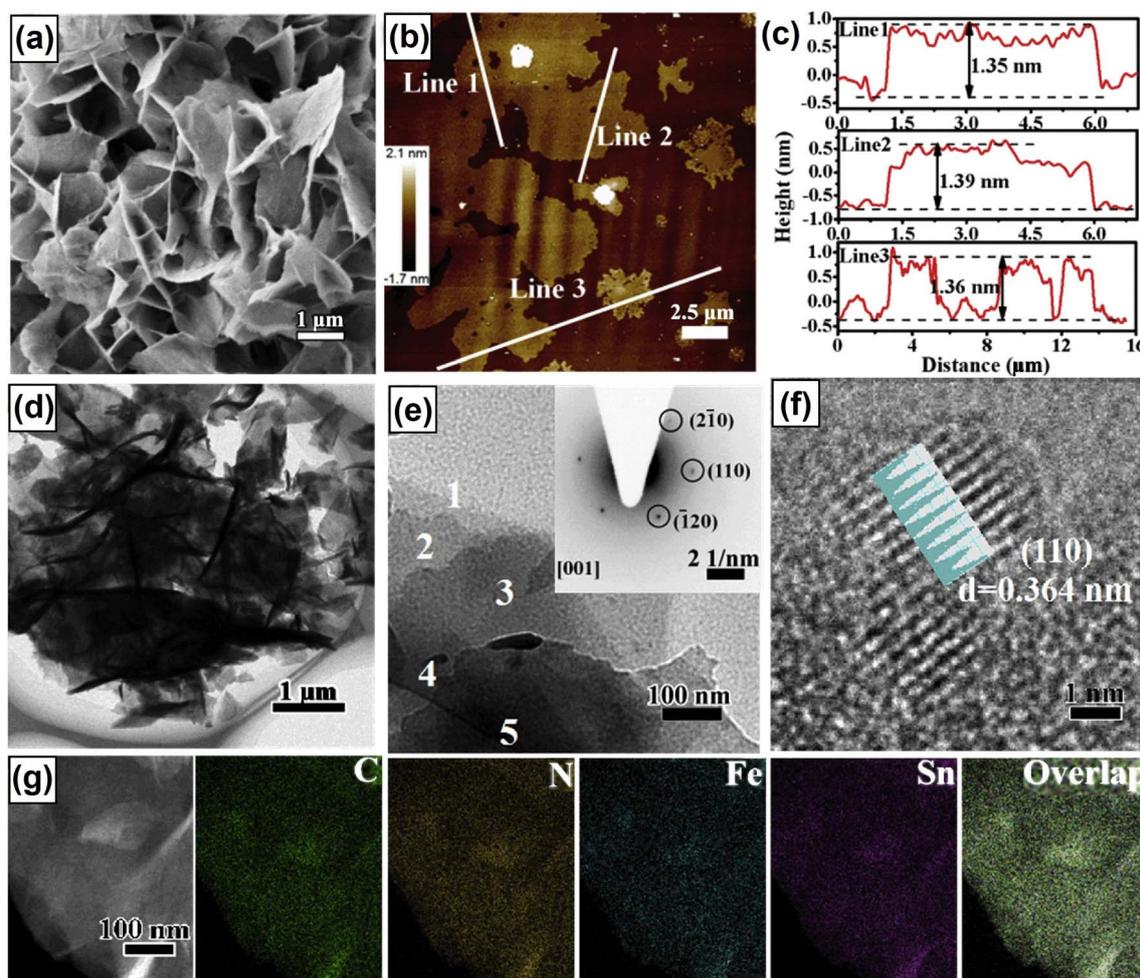

Fig. 7 Morphological and microstructural characterizations of SnFe-PBA-NSs. (a) SEM image; (b) AFM image and (c) the corresponding height profiles for the Line 1, Line 2, and Line 3 marked in (b); (d and e) HRTEM images (inset image of (e) represents the SAED pattern); (f) HRTEM image showing the lattice fringes; (g) HAADF-STEM image and corresponding EDS elemental mapping images. Reproduced with permission from ref. 42. Copyright (2022), Elsevier Inc.

for the other Ge anodes because of the kinetic limitations of the host matrix. There is a capacity recovery when the rate is returned to C/10. The coulombic efficiency in the composite anode was stabilized after performing the first five cycles, and it was averaged to ~98%. The initial performance reduction observed in the first five cycles was due to the formation of the SEI layer.

Zhang and team synthesized a few-layered stanene (Sn-ene) quantum dots having a lateral size of ~8 nm with a thickness of about 1 nm is self-reconstructed from SnFe-monolayer Prussian Blue analogue nanosheets (SnFe-PBA-NSs).[42] The system was prepared on a large scale through facile ultrasonication-controlled self-assembly combined with a fluid-flow control arrangement. The authors of this work have prepared a few-layered Sn-ene quantum dots using an *in situ* electrochemical reduction approach with SnFe-PBA-NSs as a self-sacrificial template. The structural and morphological features of the prepared SnFe-PBA-NSs were evaluated. The SEM analysis revealed that the SnFe-PBA-NSs hold ultrathin multiply interconnected NSs with lateral diameters at the micrometer scale (Fig. 7a). The mean thickness of these NSs was measured to be ~1.36 nm, estimated with the help of AFM imaging, in correlation with the theoretical thickness of 13.6 Å for mono-layer $Sn_2[Fe(CN)_6]$, verifying the single-layer characteristics of SnFe-PBA-NSs, as given in Fig. 7b and c. The microstructure of SnFe-PBA-NSs was examined using high-resolution TEM (HRTEM) and high-angle annular dark-field scanning

transmission electron microscopy (HAADF-STEM). The semi-transparent character in the HRTEM image indicates the ultrathin thickness of the SnFe-PBA-NSs monolayer, and these proposed NSs were intertwined (Fig. 7d). In addition, an HRTEM image representing several NS layers that closely touch each other is shown in Fig. 7e. The selected area electron diffraction (SAED) pattern shown in the inset graph of Fig. 7e, indexed as in-plane 2D reflections with zone axis in [001] directions, confirms the rhombohedral pattern and agrees with the XRD analysis. Here, the NS coordination polymer is sensitive to the electron beam, it introduces some degree of lattice distortion. However, the undamaged parts of HRTEM provide a clear display of lattice fringes with an interplanar spacing of 0.364 nm (Fig. 7f), corresponding to the (110) plane of SnFe-PBA. The HAADF-STEM image and the corresponding energy-dispersive spectroscopy (EDS) elemental mapping analysis for the SnFe-PBA-NSs indicate a homogeneous distribution of various elements within the material (Fig. 7g).

These Sn-ene quantum dots possess features such as abundant exposed active sites, especially edge centers, and they exhibit higher efficiency for fabricating a rechargeable battery. The authors of this work fabricated a Zn–CO_2 battery system in a flow cell configuration with 0.5 M $KHCO_3$ in a cathodic compartment pumped by CO_2. The selected anolyte was 6 M KOH + 0.02 M $Zn(CH_3COO)_2$. The CO_2 gas flow was controlled using a flow meter in order to make a flow rate through the cathodic compartment at 20 mL min^{-1}. A perfectly polished Zn
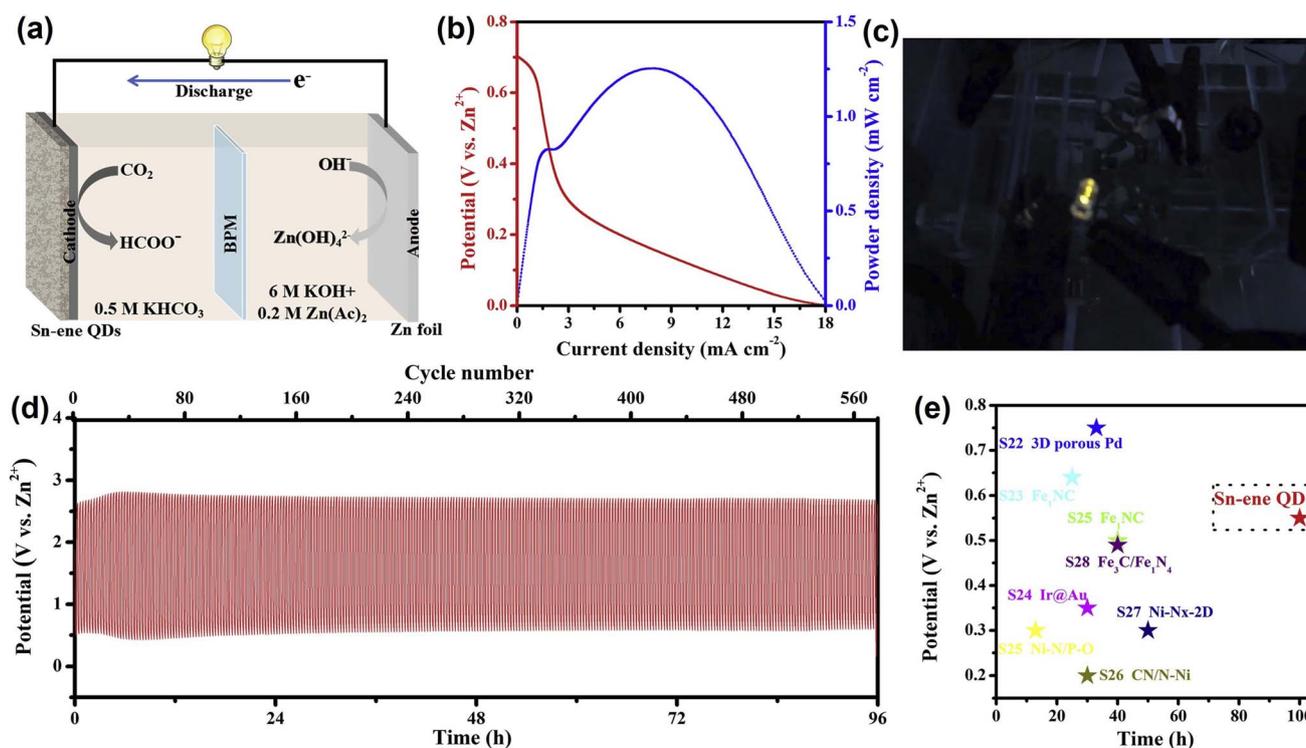

Fig. 8 Electrochemical measurements for the Zn–CO_2 battery. (a) Schematic of the Zn–CO_2 battery; (b) discharge polarization curve and variation of power density with respect to current density; (c) two Zn–CO_2 batteries connected in series powering an LED; (d) cyclic stability test results for 96 h at a constant current density of 1 mA cm^{-2}; (e) comparison of Se-ene cathode-based Zn–CO_2 battery with similar reports in the literature. Reproduced with permission from ref. 42. Copyright (2022), Elsevier Inc.

plate with an area of 2 × 3 cm² was used as the anode. With respect to the excellent carbon dioxide redox reaction (CO₂RR) characteristics, the Sn-ene quantum dots served as excellent candidates as catalysts. A schematic of the Zn–CO₂ battery is shown in Fig. 8a. The discharge polarization curve and the power density at different current densities are shown in Fig. 8b. The Zn–CO₂ battery delivered a maximum power density of 1.25 mW cm⁻² at a current density of 7.9 mA cm⁻². The practical application of this Zn–CO₂ battery was evaluated by connecting two individual batteries in series that could power a light-emitting diode (LED), as shown in Fig. 8c. Additionally, the Zn–CO₂ battery held excellent cycling stability for more than 560 cycles when performed at a current density of 1 mA cm⁻² (Fig. 8d). Fig. 8e compares the operating potential of the Sn-ene cathode-based Zn–CO₂ battery with that reported in the literature, revealing its superior performance.

The sodium-ion batteries (SIBs) are extensively studied as candidates among the various rechargeable batteries nowadays due to their high safety, low cost, and environmentally friendly nature.[43] SIBs take advantage of advantageous features such as Na resource abundance, reduced cost and lower reduction potential.[44] There are reports based on metallenes for SIBs, in order to establish its application in rechargeable batteries

beyond LIBs. Ge-ene with a higher specific surface area buffers the volume expansion in Na-ion charging/discharging. The reduced diffusion path for electrons/ions and efficient mechanical flexibility help to achieve high cyclic stability. The defect-rich structure of Gene induces improved Na ion adsorption to the active sites, thereby increasing the storage capability of SIBs. It has been reported that the Ge-ene nanosheets can be synthesized via thermal dehydrogenation of 2D hydrogenated Ge-ene (GeH) single crystals.[45] In this synthesis approach, the GeH nanosheet precursor is synthesized through the Zintl-phase CaGe₂ topochemical intercalation at a reduced temperature range, and it is further annealed at a temperature of 270 °C to remove the H layers. After subsequent annealing for 1 h at higher temperatures, Ge-ene particles were obtained from Ge-ene nanosheets. The as-prepared GeH nanosheets exhibited a mean lattice spacing of 0.332 nm. To make a comparison, the authors of this work evaluated the electrochemical characteristics of ultrathin GeH nanosheets. Ge-ene has higher H defects, and Ge particles were evaluated in a coin-type half-cell with Na metal foil as a counter electrode. The Na-ion storage characteristics of GeH, Ge-ene nanosheets and Ge particles were characterized by CV analysis at a fixed scan rate of 0.1 mV s⁻¹ in 1 M NaClO₄ electrolyte. The CV curves are shown in Fig. 9a–c for
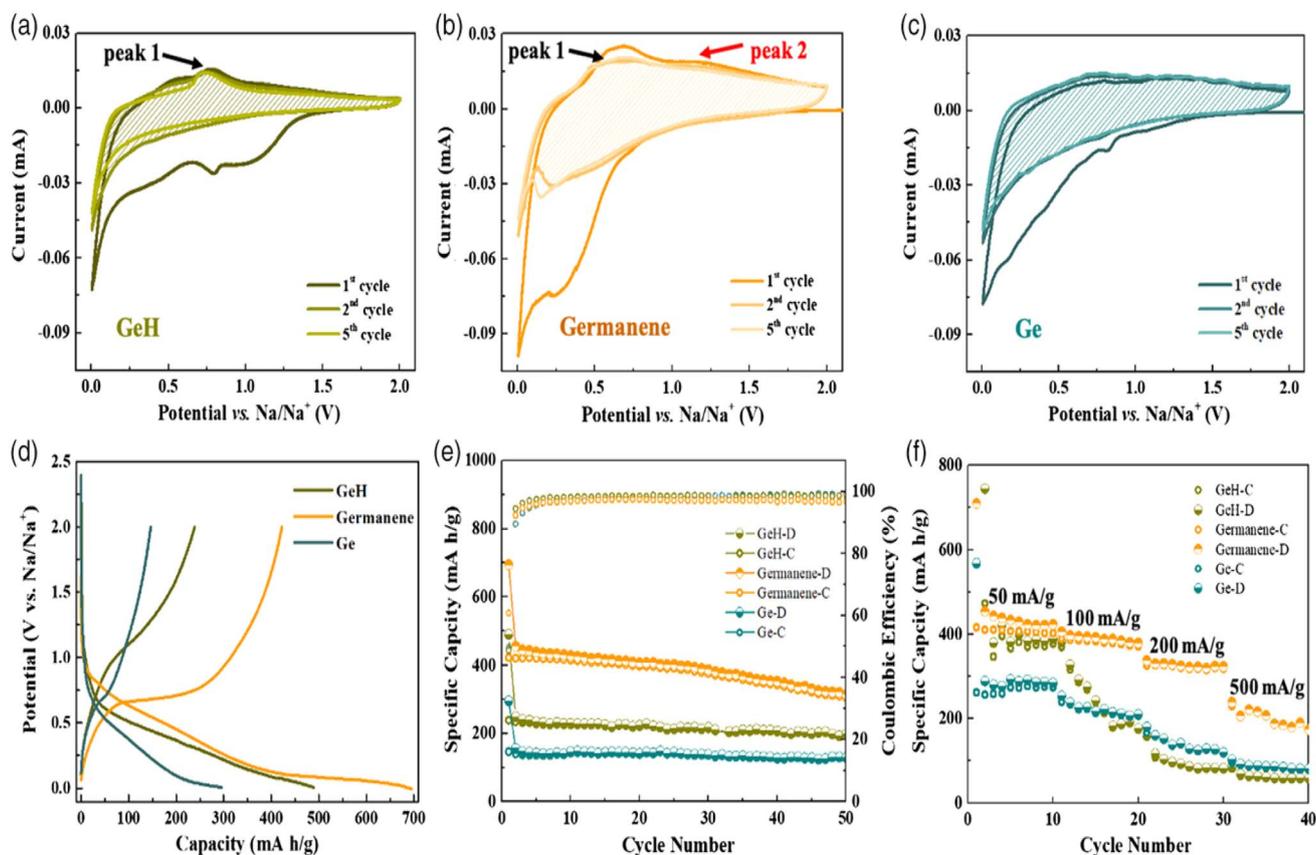

Fig. 9 Electrochemical performance evaluations of SIBs. CV curves at the 1st, 2nd and 5th cycles for (a) GeH, (b) Ge-ene nanosheets, and (c) Ge particles within a potential window of 0.01 and 2.0 V at a constant scan rate of 0.1 mV s⁻¹; (d) GCD profiles for the first cycle for Ge-ene nanosheets, GeH, and Ge particles at a constant current density of 100 mA g⁻¹; (e) plot of variation in the specific capacity and coulombic efficiency at different cycle number of various Ge-based SIBs obtained at a current density of 100 mA g⁻¹; (f) comparative analysis of rate capability of various Ge-based SIBs for 40 cycles. Reproduced with permission from ref. 45. Copyright (2021), Wiley-Verlag VCH Ltd.

GeH, Ge-ene nanosheets and Ge particles, respectively. The initial cathodic curves of the Ge-based electrodes were different from their initial cycles because of the formation of the SEI layer due to electrolyte decomposition. The CV curves of GeH (Fig. 9a) and Ge-ene nanosheets (Fig. 9b) show well-aligned redox peaks, whereas it is found to be absent in the case of Ge particles (Fig. 9c), representing different storage of Na-ion process in Ge-ene nanosheets and the GeH (intercalation process) and the Ge-particles (alloying), it is verified through experimental and theoretical procedures. In the initial discharge process, Ge-ene nanosheets (Fig. 9b) hold a broader peak centered at 0.2 V with a higher current density and a larger integrated area compared to GeH, indicating that there exists a large insertion of Na ions in Ge-ene, which is due to the removal of hydrogen atoms and the creation of abundant active sites for the storage of Na-ions. In the subsequent charging phenomena of Ge-ene, there exist two broad peaks present at 0.7 V (first peak) and 1.1 V (second peak), which reflect deintercalation through a multistep procedure of Na ions. In the case of GeH, the CV curve exhibits only a single pair of well-defined redox peaks. This is due to the presence of hydrogen atom occupation in the active sites or the hindering of the diffusion of Na ions in GeH. The CV curve of GeH and Ge-ene overlapping perfectly in subsequent cycles indicates efficient electrochemical reversibility. The GCD profiles of the GeH, Ge-ene nanosheets, and Ge particles are

shown in Fig. 9d. The Ge-ene nanosheets deliver a higher initial discharge capacity of 695 mA h g^{-1} at a current density of 0.1 A g^{-1}, in comparison with GeH (490 mA h g^{-1}) and Ge particles (296 mA h g^{-1}). Ge-ene exhibits an initial coulombic efficiency of 60.8%, whereas it was 48.8% for GeH and 49.6% for Ge particles, demonstrating the reduced irreversible capacity loss and effective cyclic stability of Ge-ene among them. The cycling and rate capability of ultrathin Ge-ene nanosheets, GeH and Ge nanoparticles are shown in Fig. 9e and f, respectively. Ge-ene maintains the specific capacity at 315 mA h g^{-1} at a 0.1 A g^{-1} after finishing 50 cycles (Fig. 9e), which is greater than GeH (197 mA h g^{-1}) and Ge nanoparticles (129 mA h g^{-1}). The possession of reduced capacity of Ge-based SIBs is due to anode material pulverization during alloying/dealloying processes, leading to the rapid fading of capacity. The rate capability of 2D Ge-ene nanosheets, GeH, and Ge particles was examined at different current densities such as 50, 100, 200, and 500 mA g^{-1}, and the variations are shown in Fig. 9f. Ultrathin Ge-ene nanosheets hold a higher rate capacity in comparison with GeH and Ge particles, and they retain a specific capacity of 342 mA h g^{-1} even at a comparatively higher current density of 500 mA g^{-1}. From these analyses, it can be inferred that the Ge-ene possesses efficient cyclic capability and rate performance. Ultrathin architecture and high H-defects induce Ge-ene nanosheet a superior candidate for energy storage
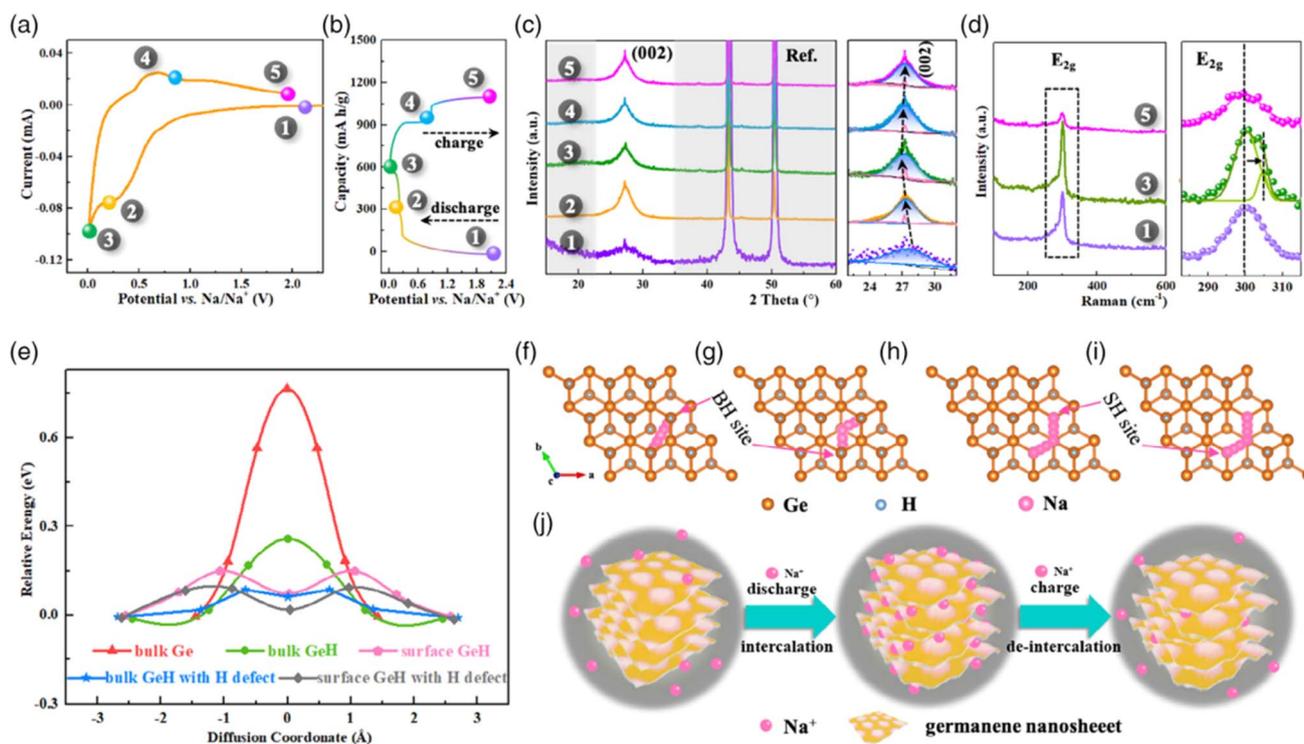

Fig. 10 *Ex situ* XRD, Raman spectroscopy and DFT studies of Ge-ene-based SIBs. (a) CV curve obtained at a scan rate of 0.1 mV s^{-1} for the first cycle within a potential range of 0.005 and 2.0 V; (b) GCD profile; (c) (left panel) *ex situ* XRD pattern at different stages of the GCD cycle and (right panel) a local enlargement of the XRD spectrum showing the peak shift of (002); (d) *ex situ* Raman spectra at different stages of the GCD cycle; (e) diffusion energy barrier comparison for Na adatoms in bulk Ge, bulk GeH, surface GeH, bulk GeH with H defect, surface GeH with H defect; DFT simulated pathways for the Na ion diffusion in (f) bulk GeH, (g) bulk GeH with H defect, (h) surface GeH, and (i) surface GeH with H defect (BH: bulk hollow; SH: surface hollow); (j) pictorial representation of Na ion intercalation in SIBs with a Ge-ene anode. Reproduced with permission from ref. 45. Copyright (2021), Wiley-Verlag VCH Ltd.

applications. The 2D ultrathin nanostructure Ge-ene also helped in establishing a more profound interfacial contact between the sheets, thereby facilitating electron/ion transportation.

To illustrate the charge storage mechanism in defect-rich Ge nanosheets, the authors of this work performed *ex situ* XRD and Raman spectroscopy to understand the sodiation/desodiation phenomena in SIBs. The various charge and discharge states during the CV analysis and GCD measurements of the SIB are shown in Fig. 10a and b, respectively. The evaluation of structural change in Ge at various charge and discharge states was examined using *ex situ* XRD, as shown in Fig. 10c. XRD spectra were recorded for the Ge anode in different voltage states as: pristine, 0.2 V (discharge), 0.005 V (discharge), 0.8 V (charge), and 2.0 V (charge) and the different colors represent the various phase compositions. For the first stage, a peak positioned at 27.8° is introduced from Ge, while peaks at 43.3° and 50.4° correspond to Cu foil. While Ge was discharged at a voltage of 0.2 V (given in the CV curve of Fig. 10a), no alterations in the XRD pattern were observed. However, when Ge is discharged at a voltage of 0.005 V, the peaks are indexed with a hexagonal Ge structure. During charging at 0.8 and 2.0 V, the diffraction pattern corresponds to Ge and the Cu foil itself. Prominently, local enlargement in the XRD patterns between the peak positions 22° and 32° was deconvoluted into two peaks, which correspond to the (002) peak in Ge (blue colour) and the (111) peak in Ge cubic (represented with pink colour), but the introduction of the (111) peak in Ge crystal is through partial crystallization during insertion/extraction. In addition, the (002) peak shifted towards the left during the discharge process due to Na^+ ion intercalation into defect-rich Ge nanosheets, (002) peak shifted toward the right. This study proposes that the storage of Na ions in Ge is due to intercalation rather than alloying, which is due to the large interlayer spacing in the ultrathin Ge nanosheets, which provides enough space for Na ion migration and transportation. This was further confirmed by *ex situ* Raman spectroscopy (Fig. 10d). When the potential from the OCP was tuned to 0.005 V, the E_{2g} mode was split prominently into two components, with one peak position remaining stable while the other peaks shifted toward slightly higher frequencies. For GeH with hydrogen defects, Na ions do not occupy defect site H among this adsorption, but the appearance of the H defect present in the material showed a reduced adsorption energy for Na ions, which makes Na atoms stable in GeH. Here, the highly stable site for the Na atom for metallic Ge is the tetrahedral site (T-site). To evaluate the diffusion of Na ions, the authors of this work used a climbing image-nudged elastic band (CI-NEB) route for the diffusion energy barrier calculation between the proposed sites, as shown in Fig. 10e. Na ions make a diffusion between two nearby SH sites on the GeH surface, with two nearby BH sites present for bulk GeH and their two nearby T-sites in the Ge metal, as shown in Fig. 10f–i. The Na ions present in Ge exhibit a higher diffusion energy barrier at 0.77 eV. The Na atom has a lower diffusion energy barrier in the GeH bulk, which is present at 0.27 eV (in the absence of H defect) and 0.1 eV (in the presence of H defect). Here, the presence of an H defect reduced the diffusion energy

barrier for Na ions in the bulk GeH phase by 0.18 eV and over the surface of GeH by 0.06 eV. Fig. 10f and g show that the appearance of the bulk H defect alters the diffusion path held by the Na atom. The Na atom diffusion during the intercalation/de-intercalation process within the Ge-ene nanosheets with H defects is schematically shown in Fig. 10j.

The buckled architecture containing Sn-ene is a highly stable candidate in comparison with the planar or puckered architecture, which possesses higher cohesive energy. Using theoretical calculations with spin-polarized DFT calculations, it was found that the Na atom is preferentially adsorbed in the hexagonal ring's H-site of Sn-ene at a distance of ~1.68 Å above the perpendicular direction.[46] The calculated adsorption energies were varied up to 0.16 eV/Na atoms per structure. A Bader charge analysis was carried out on the system and found that the loss of Na was 0.77 electrons per atom of electronic charge to the Sn-ene Sn atoms. From this study, it was found that Na adsorption with respect to a number of atoms holds the highest distortion for Sn–Sn bond length, and it was approximately 5% greater than pristine Sn-ene. These observations are significant for the use of Sn-ene for SIBs with high efficiency. With the aid of first-principle calculations, a nanomesh-structured 2D Sn-ene as an anode material for SIBs was evaluated by Wu *et al.*[47] The nanohole defects present in Sn-ene improve the binding intensity of Na ions and reduce the diffusion barrier of Na to as low as 0.15 eV following the adsorption of Na ions in bulk Sn-ene. This higher nanohole density in this nanomesh architecture promotes the adsorption of Na ions, a large theoretical capacity, and a reduced diffusion barrier. Li-ion interactions on zigzag Sn-ene doped with beryllium (Be) were evaluated using the DFT approach. By taking the Be location as a reference, there exists a symmetric structure can be created for the Be atom location. Thus, without considering the overall hole locations, only nine-hole locations were considered for the adsorption energy calculation of Li atoms on the Be-doped Sn-ene. The authors of this work observed that, concerning an increase in Li atom adsorption, there occurs a reduction in adsorption energy from the highest value of −2.17 to −1.24 eV. For the adsorption of the 60th Li atom, the adsorption energy attains a value of −1.24 eV. In addition, the open-circuit voltage of the Be-doped Sn-ene <1.16 eV. The Be-doped Sn-ene delivered a storage capacity of 200 mA h g^{-1}, in a case where the substrate with all hole locations was occupied with Li atoms. This study introduced an idea about the role of dopants in Sn-ene.

The Zn–air battery is a prominent battery technology based on the oxygen reduction reaction with slow kinetic performance. Currently, metallenes have received attention as an efficient candidate in Zn-air battery fabrication. By understanding the features of tetrametallene compounds, Zheng *et al.* synthesized PdMoCrW tetrametallene with an optimized d-band center.[48] For PdMoCrW tetrametallene, the high-valence metals Mo, Cr and W introduce water dissociation and promote protons for ORR kinetics. In addition, the electronic coupling exhibited at the interface of crystalline-amorphous optimizes the electronic structure held by Pd and achieves a downward shift in the d-band center. This makes an attenuation in O adsorption and increases ORR activity. The

PdMoCrW tetrametallene is synthesized using $(NH_4)_2PdCl_4$, $Mo(CO)_6$, $Cr(CO)_6$, $W(CO)_6$, PVP, CTAB and HCHO are dispersed in DMF solution. After stirring, the resultant solution was transferred to a Teflon-lined autoclave at a temperature of 150 °C for 12 h. The resultant product was collected via centrifugation and washed with ethanol. The resulting PdMoCrW tetrametallene was labelled as $Pd_{75.9}$ $Mo_{9.4}$ $Cr_{8.9}$ $W_{5.8}$. A pictorial illustration of the complete procedure for synthesizing PdMoCrW tetrametallene is shown in Fig. 11a. Using TEM imaging, the authors of this work found that this tetrametallene has a 2D ultrathin nanosheet morphology (Fig. 11b). The atomic ratio of Pd/Mo/Cr/W in this tetrametallene was $75.9 : 9.4 : 8.9 : 5.8$. The HRTEM images (Fig. 11c and d) indicate that the tetrametallene consists of multilayered nanosheets. Here, $Pd_{75.9}$-$Mo_{9.4}Cr_{8.9}W_{5.8}$ tetrametallene nanosheet exhibits a monolayer thickness ranging from 1.41–1.49 nm, corresponding to 6–7 atomic layers. From the HAADF-STEM image with the line scan profile as an inset image (Fig. 11e) and elemental mapping analysis (Fig. 11f–m) show Pd, Cr, Mo, and W make a uniform dispersion, which agrees with the line scan. The authors of this

work evaluated the influence of various experimental parameters on the growth mechanism of tetrametallene. The pyrolysis of carbonyl salts introduced CO, which induced the formation of nanosheets. Thus, irregularly shaped nanoparticles were introduced in the absence of carbonyl salts. The Br^- ions present in CTAB form a complex with the metal ions, thereby optimizing the reduction potential and kinetics. In the absence of CTAB, multiple polyhedrals are introduced over irregular nanosheets because of the faster reduction rate. The PVP adsorbed on the surface of the metal and the spatial cooling introduced by the long polymer introduced spatial-site blocking phenomena, thereby preventing possible agglomeration. Thus, in the absence of PVP, nanosheets are agglomerated, leading to the self-assembly of a nanoflower-like morphology. The authors of this work performed time-dependent experiments in order to understand the formation mechanism of PdMoCrW tetrametallene. For an initial reaction time of 1 minute, there exists the formation of uniformly dispersed Pd nanoparticles. When the reaction time reaches 15 minutes, these Pd nanoparticles tended to aggregate and further nucleate to form nanosheets on
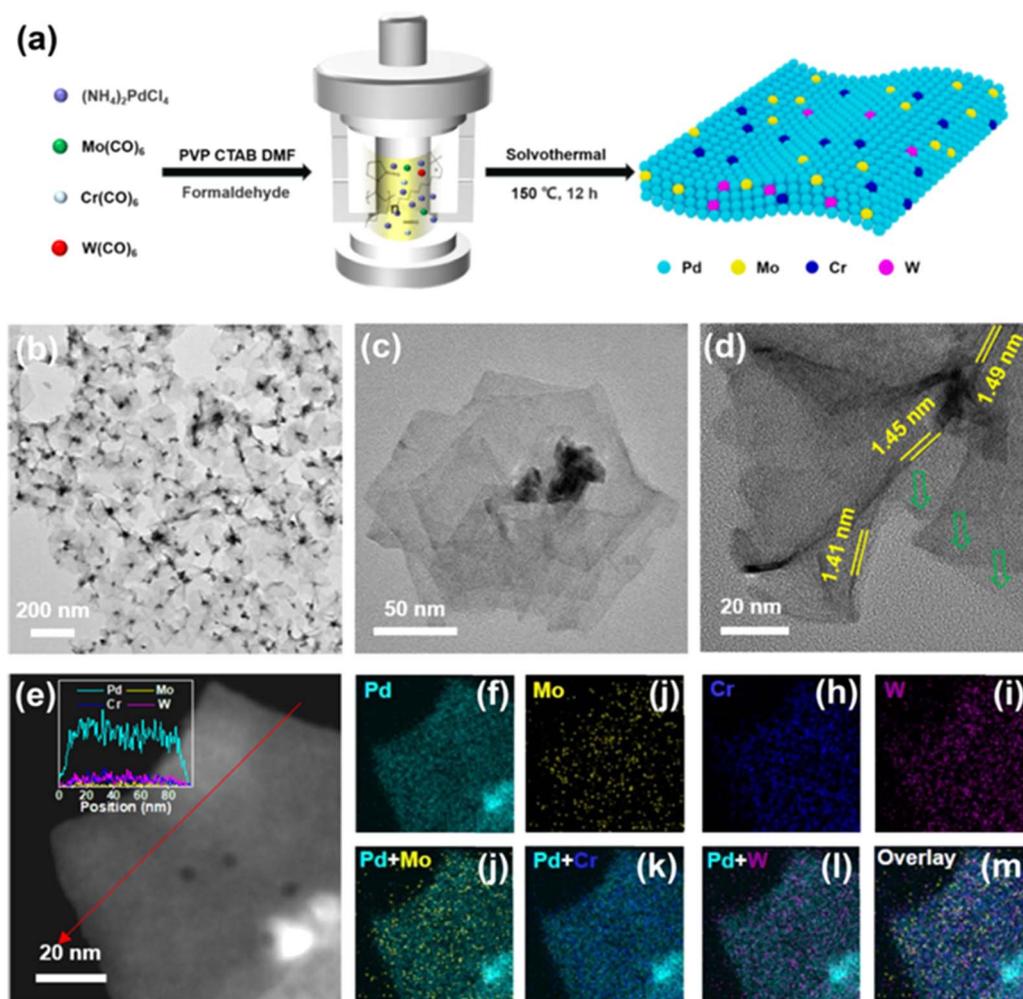

Fig. 11 (a) Schematic shows the synthesis procedure of PdMoCrW tetrametallene; (b) TEM image of PdMoCrW tetrametallene; (c and d) HRTEM images of PdMoCrW tetrametallene; (e) HAADF–STEM image (inset: line scan profile along the Red arrow) (f–m) elemental mapping images. Reproduced with permission from ref. 48. Copyright (2024), the American Chemical Society.

the edge. With a further increase in processing time from 15 to 60 minutes, there exists lateral growth of nanosheets with an increase in size, and a slow increase in the Mo, Cr, and W content occurs. This process indicates that Pd nanosheets undergo rapid growth and that incorporation by individual elements is slow. When the reaction time approaches 12 h, no prominent change is observed in the size of the nanosheet, and rapid growth of Mo, Cr, and W to 9.4%, 8.9%, and 5.8%, respectively, can be observed. This makes an indication of the consumption of the Pd precursor in the first 60 minutes, which is followed by interdiffusion and incorporation of Mo, Cr, and W in the PdMoCrW tetrametallene. From the results of this study, it can be concluded that the PdMoCrW tetrametallene was formed via a nucleation–lateral growth–atom diffusion mechanism pathway.

For the proposed mechanism, PVP coordinates with Pd^{2+} and a reduction in CTAB with formaldehyde to produce Pd nanoparticles. In due course, formaldehyde and carbonyl salts decompose at high temperatures to produce CO. CO makes preferential adsorption on the (111) crystal facet present in Pd. If there are enough CO molecules to completely cover the Pd surface, further nanosheet growth occurs along the (111) direction of the crystal facet and triggers anisotropic growth towards the formation of metallene. When the reaction time is further increased, there exists a depletion of the Pd precursors to stop the nanosheet growth, there exists a gradual incorporation and diffusion of Mo, Cr, and W atoms on the tetrametallene. The authors of this work performed electrochemical measurements using tetrametallene with a carbon (XC-72) suspension as the working electrode (glassy carbon), Hg/HgO as a reference electrode and a graphite rod as the counter electrode. CV measurements were performed in a 0.1 M KOH N_2 saturated solution at a scan rate of 50 mV s^{-1} and the ORR analysis was performed in a 0.1 M KOH O_2 saturated solution at 10 mV s^{-1}. Accelerated durability analysis was performed within a voltage range of 0.6–1.0 V vs. RHE at 100 mV s^{-1} for 10 000 cycles. The experimental analysis shows that the $Pd_{75.9}Mo_{9.4}$-$Cr_{8.9}W_{5.8}$/C electrode possesses excellent mass and specific activity of 2.81 mA mg$_{Pd}^{-1}$ at 4.05 mA cm^{-2}, which is higher than that of commercial Pt/C. The ORR activity of metallene is due to the following features: (i) the ultrathin 2D metallene curled structure induces a higher density for unsaturated active sites and increases the use of Pd atoms, (ii) the synergistic effect of crystalline-amorphous interface facilitates the redistribution of charge density and it optimizes the oxygen intermediates adsorption energy, (iii) the intrinsic electronic structure of active sites was optimized with the coordination effect and it is introduced with alloying heteroatoms such as Cr, Mo, and W, and (iv) the higher valence state hold by Cr, Mo, and W improves the surface hydrophilicity to the metallene, which accelerates H_2O activation thus provide protons to form OOH* or OH*. To evaluate the practical functionality of the prepared catalyst, the authors of this work assembled a Zn–air battery. Two similar Zn–air batteries connected in series combination delivered an open circuit voltage of 2.96 V, whereas it was 1.48 V for the single cell (Fig. 12a). A maximum specific capacity of 895 mA h kg$_{zn}^{-1}$ was exhibited by the Zn–air battery, indicating efficient energy conversion capability (Fig. 12b). Fig. 12c shows
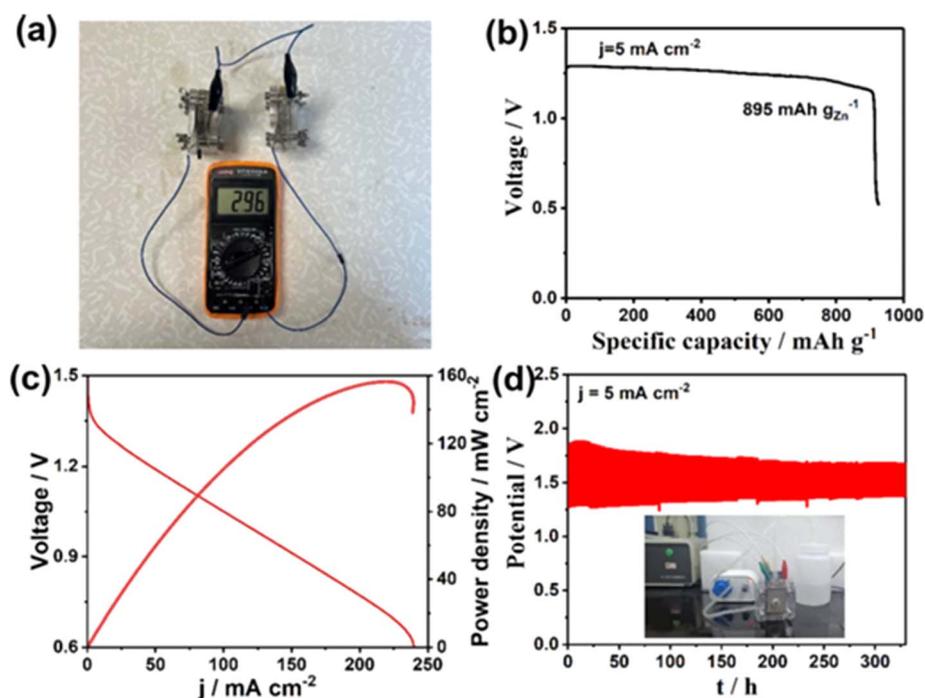

Fig. 12 (a) OCV for the series connection of two similar Zn-air batteries tested with a multimeter; (b) discharge curve at a constant current density of 5 mA cm^{-2}; (c) polarization curve and power density of Zn−air battery with respect to different current densities; (d) stability test performed for the Zn−air battery for 329 h (inset: digital photograph of the battery cycling). Reproduced with permission from ref. 48. Copyright (2024), the American Chemical Society.

that the Zn–air battery exhibits a maximum power density of 156 mW cm^{-2}. The cyclic stability of the battery was tested for 329 h, the digital photograph of the battery testing is given as an inset image in Fig. 12d, which shows good stability. This study proposes multimetallene architectures as potential candidates for Zn–air batteries.

With the aid of the molecule-metal relay catalysis approach, Zhou et al.[49] introduced rhodium-copper (RhCu) alloy metallene for nitrate conversion toward NH$_3$ at a low overpotential in a neutral solution. The RhCu catalyst exhibits efficient NH$_3$ faradaic efficiency over a potential window of −0.1 to −0.4 V. It delivers a maximum NH$_3$ faradaic efficiency of 84.8% at a reduction potential of −0.2 V in a neutral medium, which is higher than that of pristine Cu and Rh. In addition, the authors of this work demonstrated the assembly of a Zn–nitrate/ethanol battery by introducing ethanol into the electrolyte to conduct an ethanol oxidation reaction to boost the energy economy while charging. The Zn–nitrate/ethanol battery exhibited a high energy density of 117 364.6 W h kg$_{cat}$$^{-1}$ with prominent rate capability and an efficient cycling stability of ~400 cycles. Among the various metallenes, Sb is a potential candidate for rechargeable batteries because of its buckled hexagonal architecture in the layered form. It is possible to isolate an efficient monolayer/few-layered Sb through a solution-phase approach as well as a mechanical exfoliation procedure, which delivers higher stability for long-term applications. Using DFT approximations, Sengupta and team[50] evaluated the Na and Li adsorption performance on free-standing monolayer Sb sheets. The authors of this work considered a 4 × 4 supercell monolayer of Sb for evaluation. In the case of completely sodiated Sb (Na$_2$Sb), it delivers a high capacity of 320 mA h g^{-1} with a mean operation voltage of ~3.1 eV. Na had a reduced diffusion barrier of 0.114 eV for a path that covered adsorption sites having stability at the trough of the buckle, and the Γ-point induces an efficient charge/discharge rate. For the condition of a complete lithiate configuration, LiSb delivers a lower capacity of 208 mA h g^{-1}, with a mean voltage of ~2.0 eV with a large diffusion barrier of 0.38 eV. They observed that in the electron density and electron localization function plot, there exists a potential screening between the metal atoms present in 2D Sb, which provides extra stability for the lithiated/sodiated structure of Sb favourable for battery applications. Among various rechargeable batteries, Li–sulfur (Li–S) batteries achieved improved performance characteristics compared with other types. Li–S batteries have a profound interest in the availability of sulfur in nature, cost-effectiveness, environmentally friendly, and reduced toxicity. However, a suitable electrode material stands as a demerit for its exploration. Allotropes of Sb, such as α- and β-phases have semiconducting characteristics and excellent structural stability. Singh et al.[51] studied the disgusting shuttling effect hindering Li–S batteries by performing the first-principle calculation for α- and β-phases of Sb.

The authors of this work executed DFT studies with a (20 × 20 × 1) k-point for monolayer pristine Sb and at a k-point (5 × 5 × 1) for (3 × 3 × 1) and supercell (3 × 4 × 1) α-Sb and the β-Sb monolayer, respectively. The Li anode is oxidized, the electrons shift to the external thread towards the cathode and the Li ions move towards the cathode through a porous separator. Further, it reacts with sulfur at different concentrations to form Li$_2$S$_n$ (n = 1, 2, 4, 6, and 8) polysulfides. The authors of this work studied LiPS components with α-Sb and β-Sb monolayers, and the configurations with good stability were optimized. The structures optimized for pristine α- and β-Sb having PBE functional for Li$_2$S@Sb, Li$_2$S$_2$@Sb, Li$_2$S$_4$@Sb, Li$_2$S$_6$@Sb, Li$_2$S$_8$@Sb, and S$_8$@Sb are shown in Fig. 13a–f and **14a–f**, respectively. After optimizing the structures, the vertical distance between the α-Sb and β-Sb surface and the LiPS species was determined as >2.0 Å. For Li$_2$S$_n$ with long chains (n = 4, 6, and 8), Li ions shift at the hollow side of the α-Sb and β-Sb surface hexagonal arrangement and there exists a parallel orientation of the Sb monolayer.
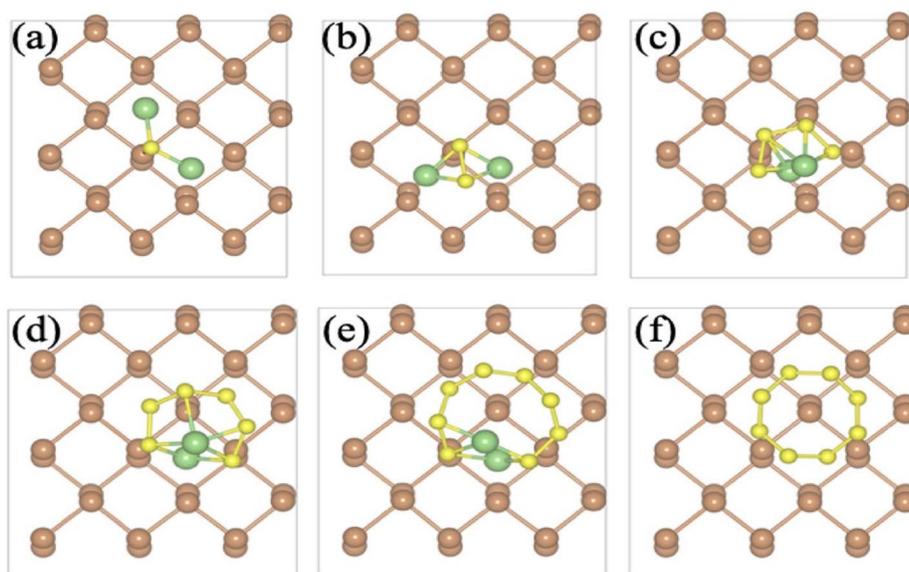
Fig. 13 Structure optimized for pristine α-Sb with the PBE functional for (a) Li$_2$S@Sb, (b) Li$_2$S$_2$@Sb, (c) Li$_2$S$_4$@Sb, (d) Li$_2$S$_6$@Sb, (e) Li$_2$S$_8$@Sb, and (f) S$_8$@Sb. Reproduced with permission from ref. 51. Copyright (2021), the American Chemical Society.

Fig. 14 Structure optimized for pristine β-Sb with the PBE functional for (a) $Li_2S@Sb$, (b) $Li_2S_2@Sb$, (c) $Li_2S_4@Sb$, (d) $Li_2S_6@Sb$, (e) $Li_2S_8@Sb$, and (f) $S_8@Sb$. Reproduced with permission from ref. 51. Copyright (2021), the American Chemical Society.

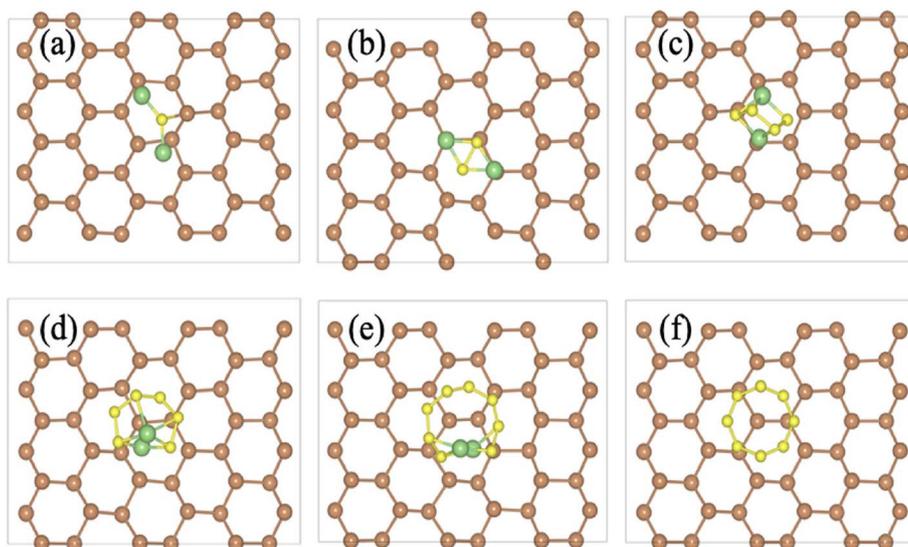However, in the short-chain ($n = 1$ and 2), Li ions make a slight displacement from the hexagonal orientation of Sb atoms present in the α-Sb and β-Sb, following the reaction between Li and S atoms. In addition, Li atoms bond with the Sb atoms of α-Sb and β-Sb with a bond length of $\sim$2.58 Å and an Sb to S bond length of 2.58 Å in the Li_2S species short chain. The bond length between Li_2S_2 species and the Sb surface is 2.83 and 2.99 Å for Sb–Li and Sb–S, respectively.

With the help of DFT simulation, Zhu *et al.*[52] evaluated the adsorption features of an oxygen-doped Sb monolayer on Li_2S_x species long chain. They observed that with an increase in adsorption energy, the oxygen-doped Sb monolayer exhibited higher adsorption of Li_2S_x long-chain species than the Sb monolayer. This increased adsorption abstracts LiPS dissolution and preserves the structural integrity of Li_2S_x species. There exists an efficient chemical interaction between Li_2S_x species and the oxygen-doped Sb layer. This study reveals the significance of heteroatom doping, particularly oxygen, in improving the performance of Sb-based battery systems. The various types of batteries assembled using metallene electrodes are listed in Table 1. In the case of newer-generation batteries, such as Li–S

and potassium-ion batteries, research is still in its infancy. Thus, designing an electrode material using metallenes with proper optimization of its structure and properties is necessary to achieve its application in rechargeable batteries to achieve performance, durability, and wide acceptability.

4. Future perspectives

By considering an analysis of the metallenes for energy storage systems, this new generation 2D material plays an efficient role in sustainable energy storage. The unique properties of metallenes, such as their large surface area, ultrathin structure, and metallic character, make them an efficient candidate for energy storage applications. Does the present review critically investigate the real-time applications of metallenes for energy storage applications to find an answer to the research question: Are the energy storage applications of metallenes a myth or reality? The literature review highlights the potential applications of metallenes for energy storage devices such as supercapacitors, rechargeable batteries, and novel battery systems assembled with the principle of electrocatalytic conversion of chemical

Table 1 Comparison of electrochemical performances of metallene-based rechargeable batteries in the literature

Battery-type	Metallenes used	Synthesis method	Morphology	Major findings	Ref.
LIB	GeH	Exfoliation	Layered architecture	Capacity: 1180 mA h g^{-1}, coulombic efficiency: 98%	41
Zn–CO$_2$ battery	Sn-ene	Ultrasonication-controlled self-assembly	Layered architecture	High-power density value of 1.25 mW cm^{-2} at 7.9 mA cm^{-2} current density	42
SIB	GeH	Topochemical intercalation with annealing	Ultrathin structure	Discharge capacity: 695 mA h g^{-1}, coulombic efficiency: 60.8%	45
Zn–air battery	Trimetallene PdMoCrW	Hydrothermal route	Ultrathin nanosheets	Specific capacity: 895 mA h kg^{-1}	48
Zn–air battery	Rhodium-copper alloy metallene	Molecule-metal relay catalysis	Layered nanosheets	Energy density: 117 364.6 W h kg^{-1}	49

compounds. 2D metallenes have not yet been explored in a wider platform; thus, the utilization of these advanced materials in energy storage systems to compete with the current demand for energy and sustainability is highly demanded. There exists a limited number of publications, especially experimental works on the application of metallenes in supercapacitors and rechargeable batteries. Beyond the thermodynamically unfavourable characteristics, the isotropic crystalline character of metals makes 2D metallenes promising for energy conversion and storage applications. From this review, the properties of 2D metallenes meet the criteria for energy storage applications and are thus not a myth. 2D metallenes are potential candidates for exploration in the field of energy storage applications. However, there are some challenges still exist with respect to the widespread exploration of 2D metallenes, which include the following:

• A suitable unified synthesis approach is mandatory to synthesize 2D metallenes in a facile, low-cost, and environmentally friendly manner with higher stability.

• The number of experimental studies conducted on the application of 2D metallenes for supercapacitors and rechargeable battery applications is much less. In general, a theoretical perspective on the adsorption/desorption of ions, and interaction/deintercalation is explored. Therefore, more experimental works on this topic are required.

• Only a limited number of 2D metallenes have been explored for energy applications, such as Ge-ene, Sn-ene, and Sb-ene. It is necessary to develop other possible 2D metallenes and evaluate their potential for energy applications.

• It is necessary to perform advanced characterization analysis for 2D metallenes to establish their growth and nucleation character and their physiochemical nature. This step helps optimize the morphology and structure of 2D metallenes.

• In the case of 2D metallenes, only single- and bimetallene compounds were explored. Similar to these, multimetallic metallenes, such as medium- and high-entropy metallenes, should be developed, and their properties should be explored for application in energy devices.

• More studies related to the influence of heteroatoms on the crystal structure of 2D metallenes are required. Doping was found to influence the crystal structure as well as the electron energy density; modulation in the same direction may be helpful in energy conversion and storage applications.

• The theoretical aspects of defect engineering in 2D metallenes to evaluate their performance modulation for energy conversion and storage applications need to be explored.

• Studies related to the synthesis of hybrids/heterostructures using 2D metallenes should be conducted. Carbon nanomaterials,[53–55] MXenes,[56–58] and metal oxide nanostructures[59,60] are good candidates to prepare hybrid electrodes. The synergistic effects of individual components in the system will help achieve the best performance in energy conversion and storage applications.

• Electronically conducting polymers are the best candidates for charge storage because of their excellent pseudocapacitive character.[61–63] Flexible nanocomposites comprising 2D metallenes and electronically conducting polymers should be prepared for next-generation flexible and wearable energy storage devices. This helps to increase the wide usage of wearable electronic gadgets that can be as thin as possible.

• A detailed investigation of the performance comparison of metallenes for novel battery systems, such as Zn-ion, K-ion, and metal–air, is to be explored.

• An in-depth analysis of the nature of the charge storage mechanism in 2D metallene-based supercapacitors is required. This will help develop other hybrid supercapacitors with high power and energy densities.

The recently explored studies on metallenes are mostly theoretical. By considering the above-mentioned facts and applying suitable modification strategies, it is possible to avoid the current drawbacks of 2D metallenes. There is an urgent need for the exploration of novel 2D metallenes for energy conversion and storage applications because they are promising materials with high electrochemical stability and durable applications. Although metallenes hold the same properties as other ultrathin 2D materials, research on these materials is still in its infancy. This is due to the limited awareness of this material to the scientific community and the difficulty associated with synthesizing approaches to prepare ultrathin 2D structures. There is great demand for 2D metallenes in the fields of physics, chemistry, materials science, energy science and engineering to develop novel devices by properly modulating their properties. The environmentally friendly nature of 2D metallenes helps in replacing other toxic materials for energy conversion and storage technologies, which eventually helps in sustainable development as well as the life of our green planet, Earth.

5. Conclusions

We have provided our perspectives on recent developments in energy storage applications of ultrathin 2D metallenes as electrode-active materials in supercapacitors, rechargeable batteries and novel battery systems assembled with the principle of electrocatalytic conversion of chemical compounds. This review reveals the unique properties that make them attractive for energy storage applications. The various synthetic strategies adopted to synthesize 2D metallenes, such as Ge-ene, Sn-ene, and Sb-ene, are explored, and their energy storage applications are evaluated. However, other types of metallenes are still in their infancy and need to be developed. The applications of 2D metallenes as electrode-active candidates in supercapacitors and rechargeable batteries were explored through performance evaluations. From our investigation, it can be inferred that the physical, chemical and electrochemical properties of 2D metallenes are important for achieving high performance when using them as electrode candidates in energy storage devices. However, few reports have described a charge storage mechanism that can enhance the stability and electrochemical performance of a battery. Multimetallenes are suitable candidates for energy storage applications, but they still need to be developed. Ultrathin structures make them suitable candidates for electrode application in the field of rechargeable batteries and supercapacitors. Because 2D

metallenes possess a larger surface area, excellent chemical and electrochemical stabilities, and an ultrathin layered structure that facilitates the rapid movement of electrolyte ions through them, thereby achieving enhanced charge storage due to diffusion-controlled charge storage. This study investigated the energy storage applications of 2D metallenes and affirms that these applications are not a myth but a reality. Developing ultrathin 2D metallenes is highly advantageous for developing sustainable electrochemical energy storage devices in the future.

Data availability

The data discussed herein can be found in the referenced articles.

Conflicts of interest

The authors declare no conflict of interest.

References

1 S. A. Thomas and J. Cherusseri, Boron carbon nitride (BCN): an emerging two-dimensional nanomaterial for supercapacitors, *J. Mater. Chem. A*, 2023, **11**(43), 23148–23187.

2 Y. Han, *et al.*, Recent progress in 2D materials for flexible supercapacitors, *J. Energy Chem.*, 2018, **27**(1), 57–72.

3 W. Bi, *et al.*, MOF-derived ultrathin carbon nanosheets integrated with telluride nanoparticles: synergistic polysulfide adsorption and catalytic sites for enhanced sulfur redox reactions, *Energy Environ. Sci.*, 2025, **18**, 1929–1940.

4 W.-X. Dong, *et al.*, Biomass-derived two-dimensional carbon materials: synthetic strategies and electrochemical energy storage applications, *FlatChem*, 2023, **37**, 100467.

5 S. A. Thomas, *et al.*, Boron carbon nitride (BCN): an emerging two-dimensional material for rechargeable batteries, *Energy Fuels*, 2024, **38**(15), 13704–13721.

6 S. A. Thomas, J. Cherusseri and D. N. Rajendran, Strategically-designed hierarchical polypyrrole-modified manganese-doped tin disulfide (SnS2) nanocomposite electrodes for supercapatteries with high specific capacity, *Electrochim. Acta*, 2024, **504**, 144910.

7 S. A. Thomas, J. Cherusseri and D. N. Rajendran, Hierarchical two-dimensional layered nickel disulfide (NiS$_2$)@ PEDOT: PSS nanocomposites as battery-type electrodes for battery-type supercapacitors with high energy density, *Electrochem*, 2024, **5**(3), 298–313.

8 S. A. Thomas, Layered two-dimensional black phosphorous-based hybrid electrodes for rechargeable batteries, *J. Energy Storage*, 2023, **73**, 109068.

9 M. Farghali, *et al.*, Strategies to save energy in the context of the energy crisis: a review, *Environ. Chem. Lett.*, 2023, **21**(4), 2003–2039.

10 S. A. Thomas, *et al.*, Strategically-Designed Environment-Friendly Tin-Based Electrodes for Sustainable Supercapatteries with High Specific Capacity, *Electrochim. Acta*, 2025, 145846.

11 P. Forouzandeh and S. C. Pillai, Two-dimensional (2D) electrode materials for supercapacitors, *Mater. Today: Proc.*, 2021, **41**, 498–505.

12 S. A. Thomas, J. Cherusseri and D. N. Rajendran, 2D nickel sulfide electrodes with superior electrochemical thermal stability along with long cyclic stability for supercapatteries, *Energy Technol.*, 2024, **12**(6), 2301641.

13 S. A. Thomas, J. Cherusseri and D. N. Rajendran, Nickel Disulfide (NiS2): A Sustainable Low-Cost Electrode Material for High-Performance Supercapacitors, *Energy Technol.*, 2024, **12**(7), 2400138.

14 S. A. Thomas, J. Cherusseri and D. N. Rajendran, Rapid synthesis of hierarchical cobalt disulfide nanostructures by microwave-assisted hydrothermal method for high performance supercapatteries, *ACS Appl. Electron. Mater.*, 2024, **6**(6), 4321–4335.

15 S. N. Kanimozhi, *et al.*, Cu-Zn layered double hydroxides as high-performance electrode for supercapacitor applications, *Electrochim. Acta*, 2024, **507**, 145106.

16 S. A. Thomas, *et al.*, Graphitic Carbon Nitride and Their Derivatives, in *Handbook of Functionalized Carbon Nanostructures: from Synthesis Methods to Applications*, Springer. 2024, pp. 1–38.

17 B. Richard, *et al.*, Minireview on fluid manipulation techniques for the synthesis and energy applications of two-dimensional MXenes: advances, challenges, and perspectives, *Energy Fuels*, 2023, **37**(10), 6999–7013.

18 S. A. Thomas and J. Cherusseri, A review of Nb2CT x MXene as an emerging 2D material: synthesis, applications in rechargeable batteries and supercapacitors, progress, and outlook, *Energy Fuels*, 2023, **37**(11), 7555–7576.

19 Y. Liu, *et al.*, Metallenes: recent advances and opportunities in energy storage and conversion applications, *ACS Mater. Lett.*, 2020, **2**(9), 1148–1172.

20 M. Liao, *et al.*, Superconductivity in few-layer stanene, *Nat. Phys.*, 2018, **14**(4), 344–348.

21 X. Chu, *et al.*, Pd-Based Metallenes for Fuel Cell Reactions, *Chem. Rec.*, 2023, **23**(2), e202200222.

22 J. Wang and H. M. Chen, Metallene pre-catalyst reconstruction for boosting catalytic performance, *Chem Catal.*, 2022, **2**(12), 3277–3279.

23 C. Cao, *et al.*, Metal–organic layers leading to atomically thin bismuthene for efficient carbon dioxide electroreduction to liquid fuel, *Angew. Chem., Int. Ed.*, 2020, **59**(35), 15014–15020.

24 C. Cao, Q. Xu and Q.-L. Zhu, Ultrathin two-dimensional metallenes for heterogeneous catalysis, *Chem Catal.*, 2022, **2**(4), 693–723.

25 Y. Liang, *et al.*, Current status and future directions of multivalent metal-ion batteries, *Nat. Energy*, 2020, **5**(9), 646–656.

26 S. H. Chung and A. Manthiram, Current status and future prospects of metal–sulfur batteries, *Adv. Mater.*, 2019, **31**(27), 1901125.

27 A. G. Olabi, *et al.*, Metal-air batteries—a review, *Energies*, 2021, **14**(21), 7373.

28 S. A. Thomas, J. Cherusseri and D. N. Rajendran, Rapid Synthesis of Hierarchical Tin Disulfide (SnS2) Nanostructures by a Microwave-Assisted Hydrothermal Method for High-Performance Supercapatteries, *ACS Appl. Electron. Mater.*, 2024, **6**(5), 3346–3361.

29 D. Bhanderi, P. Lakhani and C. K. Modi, Graphitic carbon nitride (gC3N4) as an emerging photocatalyst for sustainable environmental applications: a comprehensive review, *RSC Sustain.*, 2024, **2**, 265–287.

30 S. A. Thomas, J. Cherusseri and D. N. Rajendran, Rapid Synthesis of Hierarchical Cobalt Disulfide Nanostructures by Microwave-Assisted Hydrothermal Method for High Performance Supercapatteries, *ACS Appl. Electron. Mater.*, 2024, **6**(6), 4321–4335.

31 C. Cao, Q. Xu and Q.-L. Zhu, Ultrathin two-dimensional metallenes for heterogeneous catalysis, *Chem Catal.*, 2022, **2**, 693–723.

32 Q.-L. Zhu and Q. Xu, Immobilization of ultrafine metal nanoparticles to high-surface-area materials and their catalytic applications, *Chem*, 2016, **1**(2), 220–245.

33 Q. Xu, *et al.*, First-principles calculation of optimizing the performance of germanene-based supercapacitors by vacancies and metal atoms, *J. Phys. Chem. C*, 2020, **124**(23), 12346–12358.

34 F.-f. Zhu, *et al.*, Epitaxial growth of two-dimensional stanene, *Nat. Mater.*, 2015, **14**(10), 1020–1025.

35 Q. Zhou, *et al.*, Quantum capacitance of vacancy-defected and co-doped stanene for supercapacitor electrodes: a theoretical study, *Electrochim. Acta*, 2022, **433**, 141261.

36 Y. Xu, *et al.*, Liquid-phase exfoliation of graphene: an overview on exfoliation media, techniques, and challenges, *Nanomaterials*, 2018, **8**(11), 942.

37 E. Martínez-Periñán, *et al.*, Antimonene: a novel 2D nanomaterial for supercapacitor applications, *Adv. Energy Mater.*, 2018, **8**(11), 1702606.

38 M. Girirajan, *et al.*, Two-dimensional layered bismuthene/antimonene nanocomposite as a potential electrode material for the fabrication of high-energy density hybrid supercapacitors, *Energy Fuels*, 2022, **36**(19), 12299–12309.

39 V. K. Mariappan, *et al.*, Antimonene dendritic nanostructures: dual-functional material for high-performance energy storage and harvesting devices, *Nano Energy*, 2020, **77**, 105248.

40 D. K. Sharma, *et al.*, Mono and bi-layer germanene as prospective anode material for Li-ion batteries: a first-principles study, *Comput. Condens. Matter*, 2018, **16**, e00314.

41 A. C. Serino, *et al.*, Lithium-ion insertion properties of solution-exfoliated germanane, *ACS Nano*, 2017, **11**(8), 7995–8001.

42 M. Zhang, *et al.*, Few-atom-layer metallene quantum dots toward CO2 electroreduction at ampere-level current density and Zn-CO2 battery, *Chem Catal.*, 2022, **2**(12), 3528–3545.

43 J.-Y. Hwang, S.-T. Myung and Y.-K. Sun, Sodium-ion batteries: present and future, *Chem. Soc. Rev.*, 2017, **46**(12), 3529–3614.

44 M. D. Slater, *et al.*, Sodium-ion batteries, *Adv. Funct. Mater.*, 2013, **23**(8), 947–958.

45 N. Liu, *et al.*, Germanene Nanosheets: Achieving Superior Sodium-Ion Storage via Pseudointercalation Reactions, *Small Struct.*, 2021, **2**(10), 2100041.

46 A. Swarup, Electrochemical properties of stanene as an efficient anode material for Na-ion batteries, *Comput. Condens. Matter*, 2018, **14**, 84–88.

47 L. Wu, *et al.*, Stanene nanomeshes as anode materials for Na-ion batteries, *J. Mater. Chem. A*, 2018, **6**(17), 7933–7941.

48 Z. Zheng, *et al.*, Crystalline–Amorphous Heterophase PdMoCrW Tetrametallene: Highly Efficient Oxygen Reduction Electrocatalysts for a Long-Term Zn–Air Battery, *Langmuir*, 2024, **40**(21), 11307–11316.

49 J. Zhou, *et al.*, Constructing molecule-metal relay catalysis over heterophase metallene for high-performance rechargeable zinc-nitrate/ethanol batteries, *Proc. Natl. Acad. Sci. U. S. A.*, 2023, **120**(50), e2311149120.

50 A. Sengupta and T. Frauenheim, Lithium and sodium adsorption properties of monolayer antimonene, *Mater. Today Energy*, 2017, **5**, 347–354.

51 D. Singh, *et al.*, Antimonene allotropes α-and β-phases as promising anchoring materials for lithium–sulfur batteries, *Energy Fuels*, 2021, **35**(10), 9001–9009.

52 V. Zhu and X. Luo, Oxygen-doped antimonene monolayer as a promising anchoring material for lithium–sulfur batteries: a first-principles study, *RSC Adv.*, 2023, **13**(43), 30443–30452.

53 S. A. Thomas, J. Cherusseri and D. N. Rajendran, Recent progresses in the synthesis and strategic designs of sustainable carbon-based fibrous electrodes for flexible batteries, *RSC Sustain.*, 2025, **3**(1), 219–242.

54 S. A. Thomas, J. Cherusseri and D. N. Rajendran, Recent advancements on carbon fibers-based sustainable electrodes for flexible and wearable supercapacitors, *RSC Sustain.*, 2024, **2**, 2403–2443.

55 S. A. Thomas, J. Cherusseri and D. N. Rajendran, Functionalized Carbon Nanostructures for Hydrogen Storage, in *Handbook of Functionalized Carbon Nanostructures: from Synthesis Methods to Applications*, Springer, 2024, pp. 1471–1509.

56 M. Zaed, *et al.*, Utilization of recycled materials for low-cost MXene synthesis and fabrication of graphite/MXene composite for enhanced water desalination performance, *Sep. Purif. Technol.*, 2025, **354**, 129055.

57 M. Zaed, *et al.*, Synthesis of Ti3C2Tx MXene@ Carbon-Enhanced cellulose fiber composite-based photothermal absorber for sustainable water desalination, *Mater. Today Sustain.*, 2024, **28**, 100971.

58 M. Zaed, *et al.*, Unlocking desalination's potential: harnessing MXene composite for sustainable desalination, *Chem. Eng. J.*, 2024, **500**, 156910.

59 M. R. Pallavolu, *et al.*, Scalable synthesis of binder-free hierarchical MnCo2O4 nanospikes/Ni(OH)2 nanosheets

composite electrodes for high-capacity supercapatteries, *J. Energy Storage*, 2023, **73**, 108999.

60 S. A. Thomas, J. Cherusseri and M. Khalid, A comprehensive review on tungsten oxide nanostructures-based electrochromic supercapacitors and machine learning models for design and process parameter optimization, *Energy Storage*, 2023, **5**(8), e499.

61 J. Cherusseri and K. K. Kar, Recent progress in nanocomposites based on carbon nanomaterials and electronically conducting polymers, *Polymer nanocomposites based on inorganic and organic nanomaterials*, 2015, pp. 229–256.

62 J. Cherusseri, *et al.*, Polymer-based composite materials: characterizations, *Composite Materials: Processing, Applications, Characterizations*, 2017, pp. 37–77.

63 S. A. Thomas, J. Cherusseri and D. N. Rajendran, A Minireview on Polyurethane-Based Flexible Electrodes for Wearable Supercapacitors: Strategies, Syntheses and Electrochemical Performance Evaluations, *Energy Fuels*, 2024, **39**(1), 2–18.

© 2025 The Author(s). Published by the Royal Society of Chemistry